

FEDERAL UNIVERSITY OF SÃO CARLOS
EXACT AND TECHNOLOGY SCIENCES CENTER
GRADUATE PROGRAM IN CHEMICAL ENGINEERING

ROBERTA RESENDE MACIEL DA SILVA

**Photocatalytic degradation of organic pollutants through
peroxymonosulfate activation: Photocatalysts and reaction mechanisms**

**Degradação fotocatalítica de poluentes orgânicos pela ativação do
peroximonosulfato: Fotocatalisadores e mecanismos de reação**

SÃO CARLOS
2023

ROBERTA RESENDE MACIEL DA SILVA

**Photocatalytic degradation of organic pollutants through
peroxymonosulfate activation: Photocatalysts and reaction mechanisms**

**Degradação fotocatalítica de poluentes orgânicos pela ativação do
peroximonosulfato: Fotocatalisadores e mecanismos de reação**

Ph.D. thesis presented to the Graduation Program in Chemical Engineering of the Federal University of São Carlos as part of the requirements to obtain the title of Ph.D. in Chemical Engineering, in the field of Research and Development of Chemical Processes.

Advisor: Prof. Dr. Luís Augusto Martins Ruotolo

Co-advisor: Prof. Dr. Francisco Guilherme Esteves Nogueira

SÃO CARLOS

2023



UNIVERSIDADE FEDERAL DE SÃO CARLOS

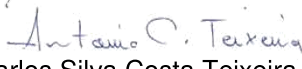
Centro de Ciências Exatas e de Tecnologia
Programa de Pós-Graduação em Engenharia Química

Folha de Aprovação

Defesa de Tese de Doutorado da candidata Roberta Resende Maciel da Silva, realizada em 30/06/2023.

Comissão Julgadora:


Prof. Dr. Luis Augusto Martins Ruotolo (UFSCar)


Prof. Dr. Antonio Carlos Silva Costa Teixeira (USP)


Profa. Dra. Elaine Cristina Paris (EMBRAPA)

Prof. Dr. Francisco Guilherme Esteves Nogueira (UFSCar)

Prof. Dr. Márcio César Pereira (UFVJM)

ACKNOWLEDGEMENTS

Once, I heard something that made me reflect on my academic trajectory: Data is never about just one person; it is about many people. This statement reminded me of my gratitude towards everyone who contributed in some way to the development of this work.

First, I would like to thank the Federal University of São Carlos (UFSCar) and the Department of Chemical Engineering for allowing me to pursue my doctorate. In addition, this work would not have been possible without the financial support of the National Council for Scientific and Technological Development (CNPq) and the company Opersan (grant #142087/2019- 0). I would also like to thank the Coordination for the Improvement of Higher Education Personnel (CAPES), which awarded me a six-month scholarship abroad (grant #88887.571964/2020-00).

Apart from my own efforts, the success of this thesis was also granted by the support and guideline of my supervisors, Prof. Dr. Luís Augusto M. Ruotolo and Prof. Dr. Francisco Guilherme E. Nogueira. I appreciate your unfailing support and assistance. I would like to extend my thanks to Dr. Ana Bahamonde from the Institute of Catalysis and Petrochemistry and Prof. Dr. Roberto Rosal from the University of Alcalá, who welcomed me so warmly into their laboratories in Spain and generously shared their knowledge and expertise with me.

Besides my advisors, I am grateful to Prof. Dr. Antonio Carlos S. C. Teixeira, Dr. Carlos Henrique M. Fernandes, Dr. Géssica O. S. Santos, Dr. Elaine Cristina Paris, and Prof. Dr. Márcio César Pereira for accepting to be members of my qualification and defense committees and for their insightful contributions to the improvement of this work.

A heartfelt thank you to Laura, Jéssica, and Rogério. I feel extremely lucky to have had the chance to meet you during this journey. Thank you for being exactly the way you are and helping me with so much kindness. Honestly, I would not have been able to complete this work without you.

To all my friends and colleagues: Kamilla, Melissa, Aline, Belle, Duda, Kaíque, Renato, Alyne, Lúrima, Larissa, Isa, Camila, Letícia, Cássia, Vitória, Luana, Patrícia, João, Priscila, Carlos, Chizoba, Ana, and Kaio, thank you for your help with data processing, feedback sessions, moral support, and joyful moments.

Last but not least, I would like to express my gratitude to my family, especially my parents, Ândrea and Roberto; my grandparents, Nelia and Eckner; my uncle André;

my sister, Neliane (*in memoriam*) and my brother, Lucas. Their love and belief in me have kept my spirit and motivation high throughout all these years.

RESUMO

A poluição da água por compostos orgânicos tornou-se uma preocupação crescente em todo o mundo, trazendo riscos tanto para a saúde humana quanto para o meio ambiente. Os rápidos avanços nas indústrias farmacêuticas e na agricultura certamente melhoraram nossa qualidade de vida, no entanto, a liberação descontrolada dos produtos farmacêuticos e pesticidas nos corpos d'água tornou-se um problema grave. Mesmo em quantidades mínimas esses poluentes têm um impacto prejudicial na saúde humana e representam uma ameaça ao equilíbrio dos ecossistemas aquáticos. Portanto, há uma necessidade urgente em se desenvolver tecnologias capazes de remover de forma eficiente esses poluentes das águas residuais. Com o objetivo de contribuir para a solução deste problema, este trabalho de tese concentrou-se em explorar o potencial de duas novas abordagens baseadas na tecnologia de ativação fotocatalítica do peroximonosulfato (PMS) para aplicação na remediação de águas contaminadas por poluentes orgânicos.

Na tentativa de desenvolver processos menos onerosos para aplicações industriais, o fotocatalisador Co_3O_4 foi utilizado sob irradiação de luz solar para ativação do PMS para degradação do pesticida imidacloprida (IMD) em um reator de fluxo contínuo. Sob condições otimizadas, uma fotodegradação de 99% do IMD foi alcançada após duas horas de operação. O excelente desempenho do processo $\text{Co}_3\text{O}_4/\text{PMS}/\text{irradiação solar}$ foi atribuído à ativação sinérgica do PMS pelas espécies Co^{2+} e Co^{3+} presentes no Co_3O_4 e pelo componente ultravioleta (UV) da luz solar, seja na fase homogênea ou após a adsorção do PMS pelo Co_3O_4 . Foi constatado que o mecanismo de degradação do IMD no sistema $\text{Co}_3\text{O}_4/\text{PMS}/\text{irradiação solar}$ envolve a formação de diferentes espécies reativas oxidativas ($^1\text{O}_2$, $\text{O}_2^{\bullet-}$, e $\text{SO}_4^{\bullet-}$), as quais foram responsáveis pela oxidação do pesticida.

Em uma segunda abordagem, a heteroestrutura $g\text{-C}_3\text{N}_4/\text{NiFe}_2\text{O}_4$ foi utilizada para ativar o PMS sob luz visível (LV) para aplicação na degradação de uma água residual simulada contendo o antibiótico cloridrato de tetraciclina (TCH) como molécula modelo de poluente orgânico. Os testes fotocatalíticos revelaram que o sistema $\text{NiFe}_2\text{O}_4/g\text{-C}_3\text{N}_4/\text{PMS}/\text{LV}$ foi bem sucedido na remoção do TCH em uma ampla faixa de pH e na presença de diferentes ânions comumente encontrados em águas residuais. O desempenho superior do compósito na degradação do TCH comparado aos óxidos puros foi atribuído ao sinergismo entre a heterojunção e a ativação do PMS, que possibilitou a geração de múltiplas espécies oxidantes ($^1\text{O}_2$, $\text{O}_2^{\bullet-}$, e HO^\bullet), responsáveis pela degradação

efetiva do TCH. Além da rápida cinética de degradação, também vale destacar as propriedades magnéticas da heteroestrutura que facilitaram a separação do fotocatalisador para fins de reuso.

ABSTRACT

Water pollution from organic compounds has become a growing concern worldwide due to the risks imposed on human health and the environment. The rapid advancements in the pharmaceutical and agricultural industries have certainly improved our quality of life; however, the uncontrolled release of pharmaceuticals and pesticides into water bodies has become a serious problem. Even in small quantities, these pollutants have a detrimental impact on human health and pose a threat to the balance of aquatic ecosystems. Therefore, there is an urgent need to develop technologies that can efficiently remove these pollutants from wastewater. To address this problem, this thesis work focused on exploring the potential of two novel approaches based on the photocatalytic activation of peroxymonosulfate (PMS) for application in the remediation of water contaminated with organic compounds.

In an attempt to develop cost-effective processes for industrial applications, the Co_3O_4 photocatalyst was applied to capture solar light to activate PMS for the degradation of the pesticide imidacloprid (IMD) in a continuous flow reactor. Under optimized conditions, 99% IMD photodegradation was achieved after two hours of operation. The outstanding performance of the Co_3O_4 /PMS/solar irradiation process was attributed to the synergistic activation of PMS by Co^{2+} and Co^{3+} species in the Co_3O_4 catalyst and the ultraviolet (UV) component of solar irradiation, in either the homogeneous phase or after PMS adsorption onto Co_3O_4 . It was found that the degradation mechanism of IMD in the Co_3O_4 /PMS/solar irradiation system involved the formation of different oxidative reactive species ($^1\text{O}_2$, $\text{O}_2^{\bullet-}$, and $\text{SO}_4^{\bullet-}$), which were responsible for the oxidation of the pesticide.

In a second approach, the g- C_3N_4 /NiFe₂O₄ heterostructure was used to activate PMS under visible light (VL), for application in the degradation of a simulated wastewater containing tetracycline hydrochloride (TCH) as a model molecule of an organic pollutant. The photocatalytic tests revealed that the NiFe₂O₄/g- C_3N_4 /PMS/VL system was successful in removing TCH over a wide pH range and in the presence of different anions commonly found in wastewaters. The superior degradation performance observed for the composite, compared to the pure oxides, was attributed to the synergism between heterojunction photocatalysis and PMS activation, generating the highly oxidizing $^1\text{O}_2$, $\text{O}_2^{\bullet-}$, and HO^\bullet species, responsible for effective degradation of TCH.

Besides the fast kinetics, it also should be highlighted that the magnetic properties of the heterostructure facilitated separation of the photocatalyst for the purpose of reuse.

SUMMARY

CHAPTER 1	1
INTRODUCTION	1
1.1. Problem Statement.....	1
1.2. Literature Review	3
1.2.1. Peroxymonosulfate-based advanced oxidation processes (PMS-AOP)	3
1.2.2. Heterogeneous photocatalytic activation of PMS	7
1.2.2.1. Cobalt oxide (Co ₃ O ₄).....	8
1.2.2.2. Carbon nitride (g-C ₃ N ₄).....	9
1.3. Objectives and Thesis Outline	11
CHAPTER 2.....	13
PEROXYMONOSULFATE ACTIVATION BY Co ₃ O ₄ COATINGS FOR IMIDACLOPRID DEGRADATION IN A CONTINUOUS FLOW-CELL REACTOR UNDER SIMULATED SOLAR IRRADIATION	13
2.1. Introduction	13
2.2. Experimental.....	15
2.2.1. Reagents	15
2.2.2. Synthesis and characterization of Co ₃ O ₄ nanoparticles.....	15
2.2.3. Fabrication and characterization of Co ₃ O ₄ coatings.....	16
2.2.4. Continuous degradation of imidacloprid in a flow-cell system.....	16
2.2.5. Analytical procedures	19
2.3. Results and discussion	19
2.3.1. Co ₃ O ₄ characterizations	19
2.3.2. Continuous degradation of IMD by Co ₃ O ₄ in the presence of PMS and solar irradiation	22
2.3.3. Mechanism of IMD degradation by Co ₃ O ₄ /PMS/solar irradiation.....	27
2.3.4. Pathway of IMD degradation by Co ₃ O ₄ /PMS/solar irradiation.....	29

2.4. Conclusions	31
CHAPTER 3.....	33
PEROXYMONOSULFATE ACTIVATION BY MAGNETIC g-C ₃ N ₄ /NiFe ₂ O ₄ FOR TETRACYCLINE HYDROCHLORIDE DEGRADATION UNDER VISIBLE LIGHT	33
3.1. Introduction	33
3.2. Experimental.....	35
3.2.1. Reagents	35
3.2.2. Synthesis and characterization of the g-C ₃ N ₄ , NiFe ₂ O ₄ , and g-C ₃ N ₄ / NiFe ₂ O ₄ photocatalysts	35
3.2.3. Photocatalytic experiments.....	36
3.3. Results and discussion	37
3.3.1. g-C ₃ N ₄ /NiFe ₂ O ₄ characterizations	37
3.3.2. Photocatalytic activity evaluation.....	42
3.3.3. Mechanism of TCH degradation by the CN/NFO/PMS/VL system.....	45
3.4. Conclusions	48
CHAPTER 4.....	49
CONCLUSIONS AND SUGGESTIONS FOR FUTURE WORKS	49
REFERENCES	51

LIST OF TABLES

Table 1.1. Characteristics of PMS.....	5
Table 2.1. Summary of the textural properties of the Co_3O_4	20
Table 2.2. IMD degradation intermediates in the Co_3O_4 /PMS/SI process, detected by HRMS-HPLC.....	30
Table 3.1. TCH degradation efficiencies achieved using different photocatalytic/PMS systems under visible light irradiation.....	45

LIST OF FIGURES

Figure 1.1. Different types of AOP that have been used for the degradation of organic pollutants. Adapted from [25].	4
Figure 1.2. Number of publications (a) and citations (b) per year since 1996 based on the search for “peroxymonosulfate” in the Web of Science (Access in June 2023).	4
Figure 1.3. Different methods for activating PMS. Adapted from [27].	6
Figure 1.4. PMS activation by photogenerated electrons. Adapted from [15].	8
Figure 2.1. Schematic representation of the experimental arrangement used for IMD degradation: (1) reservoir containing the pesticide and PMS, (2) peristaltic pump, (3) bubble trap, (4) catalytic film + flow cell (7.7 cm ³ , Sigma-Aldrich), (5) Xe arc lamp (15 cm above the flow cell), and (6) reservoir for the treated solution.	17
Figure 2.2. Emission spectra of the Heraeus TQ 150 Xe arc lamp.	17
Figure 2.3. Emission spectra of the Heraeus TQ Xe arc lamp with R3114 UV filter.	18
Figure 2.4. XRD pattern of the as-prepared Co ₃ O ₄ nanoparticles.	20
Figure 2.5. N ₂ adsorption-desorption isotherm (a), cumulative pore volume (b) and pore size (c) distributions of the as-synthesized Co ₃ O ₄ nanoparticles.	21
Figure 2.6. Top-view SEM images of the glass microfiber filter substrate (a) and the Co ₃ O ₄ -coated substrate fabricated by vacuum filtration (b-c).	21
Figure 2.7. UV-Vis absorption spectrum (a) and Tauc plot (b) for the as-prepared Co ₃ O ₄ nanoparticles.	22
Figure 2.8. IMD degradation curves under different reaction conditions: —●— PMS only; —○— photolysis; —●— photocatalysis (in the absence of PMS); —●— PMS and SI; —●— Co ₃ O ₄ and PMS in the dark; —●— Co ₃ O ₄ and PMS under SI. Experimental conditions: 2.5 mg _{IMD} L ⁻¹ ; 0.4 mg _{catalyst} cm ⁻² ; 0.2 g _{PMS} L ⁻¹ ; $u = 0.1$ mL min ⁻¹ .	24
Figure 2.9. Effect of the PMS concentration (a-c) with a flow rate of 0.2 mL min ⁻¹ on IMD degradation in the dark and under solar irradiation. Experimental conditions: 2.5 mg _{IMD} L ⁻¹ ; 0.4 mg _{catalyst} cm ⁻² .	25
Figure 2.10. Effect of the flow rate (d-f) with PMS concentration of 0.2 g _{PMS} L ⁻¹ on IMD degradation in the dark and under solar irradiation. Experimental conditions: 2.5 mg _{IMD} L ⁻¹ ; 0.4 mg _{catalyst} cm ⁻² .	26
Figure 2.11. Effect of different irradiation types on IMD degradation. Experimental conditions: 2.5 mg _{IMD} L ⁻¹ ; 0.4 mg _{catalyst} cm ⁻² ; $u = 0.1$ mL min ⁻¹ .	27

Figure 2.12. IMD degradation using the $\text{Co}_3\text{O}_4/\text{PMS}/\text{SI}$ approach in the presence of different radical scavenger species. Experimental conditions: $2.5 \text{ mg}_{\text{IMD}} \text{ L}^{-1}$; $0.4 \text{ mg}_{\text{catalyst}} \text{ cm}^{-2}$; $0.2 \text{ g}_{\text{PMS}} \text{ L}^{-1}$; $u = 0.1 \text{ mL min}^{-1}$. Scavenger concentration: 1 mM ; solar irradiation: 18.2 W m^{-2}	28
Figure 2.13. IMD degradation pathway in the $\text{Co}_3\text{O}_4/\text{PMS}/\text{SI}$ process.....	31
Figure 3.1. XRD patterns of $\text{g-C}_3\text{N}_4$, NiFe_2O_4 , and $\text{g-C}_3\text{N}_4/\text{NiFe}_2\text{O}_4$	37
Figure 3.2. TEM (a-c) and HRTEM images (d-f) of $\text{g-C}_3\text{N}_4/\text{NiFe}_2\text{O}_4$	38
Figure 3.3. XPS survey spectrum (a), and C 1s (b), N 1s (c), O 1s (d), Fe 2p (e), and Ni 2p (f) high resolution spectra of $\text{g-C}_3\text{N}_4/\text{NiFe}_2\text{O}_4$	39
Figure 3.4. UV-Vis absorption spectra (a) and Tauc plots (b) of the photocatalysts. ...	40
Figure 3.5. PL spectra of the photocatalysts.....	41
Figure 3.6. Magnetization hysteresis loops of NiFe_2O_4 and $\text{g-C}_3\text{N}_4/\text{NiFe}_2\text{O}_4$	41
Figure 3.7. Normalized TCH degradation over time, under different reaction conditions.	42
Figure 3.8. Reuse tests using CN/NFO.....	43
Figure 3.9. Effect of initial pH on TCH degradation performance. Note: Control refers to the TCH solution without pH adjustment.....	43
Figure 3.10. Effects of NO_3^- , SO_4^{2-} , Cl^- , and HCO_3^- on TCH degradation performance. Note: Control refers to the TCH solution without addition of anions.	44
Figure 3.11. Effects of different quenchers on TCH degradation using the CN/NFO/PMS/VL system. Note: Control refers to the TCH solution without quenchers.	46
Figure 3.12. Proposed mechanism for TCH degradation by NFO/CN composite in presence of PMS and visible light.....	48

ABBREVIATIONS

AOCs	Anthropogenic organic compounds
AOP	Advanced oxidation processes
BDDT	Brunauer-Deming-Deming-Teller
BET	Brunauer-Emmett-Teller
CB	Conduction band
CN	Carbon nitride
DLS	Dynamic light scattering
DNA	Deoxyribonucleic Acid
DO	Dissolved oxygen
DRS	Diffuse reflectance spectroscopy
ECOSAR	Ecological Structure Activity Relationships Program
EPA	Environmental Protection Agency
FFA	Furfuryl alcohol
HPLC	High performance liquid chromatography
HRMS	High-resolution mass spectrometry
HRTEM	High-resolution transmission electron microscopy
ICP-OES	Inductively coupled plasma optical emission spectroscopy
ICSD	Inorganic Crystal Structure Database
IMD	Imidacloprid
NFO	Nickel ferrite
NOCs	Natural organic compounds
NPs	Nanoparticles
p-BQ	p-benzoquinone
PL	Photoluminescence
PMS	Peroxymonosulfate
ROS	Reactive oxygen species
SEM	Scanning electron microscopy
SI	Solar irradiation
TBA	Tert-butyl alcohol
TCH	Tetracycline hydrochloride
TCs	Tetracyclines

TEM	Transmission electron microscopy
TOC	Total organic carbon
UV	Ultraviolet
VB	Valence band
VI	Visible irradiation
VL	Visible light
VSM	Vibrating sample magnetometer
XPS	X-ray photoelectron spectroscopy
XRD	X-ray diffraction

SYMBOLS

A_{external}	External surface area	$\text{m}^2 \text{g}^{-1}$
A_{micro}	Micropore surface area	$\text{m}^2 \text{g}^{-1}$
C_0	Initial pollutant concentration	mg L^{-1}
C	Pollutant concentration at time t	mg L^{-1}
E_g	Band gap energy	eV
E^0	Energy of free electrons on the hydrogen scale	eV
$h\nu$	Photon energy	eV
S_{BET}	Specific surface area calculated by Brunauer-Emmett-Teller equation	$\text{m}^2 \text{g}^{-1}$
t	Residence time	min
u	Flow rate	mL min^{-1}
$V_{\text{micropores}}$	Volume of micropores	$\text{cm}^3 \text{g}^{-1}$
$V_{\text{mesopores}}$	Volume of mesopores	$\text{cm}^3 \text{g}^{-1}$
$V_{\text{macropores}}$	Volume of macropores	$\text{cm}^3 \text{g}^{-1}$
V_{total}	Total volume	$\text{cm}^3 \text{g}^{-1}$
ζ -potential	Zeta potential	mV
X	Absolute electronegativity	-
λ	Wavelength	nm

CHAPTER 1

INTRODUCTION

1.1. Problem Statement

One of the biggest challenges in the modern world is the availability of clean, safe, and affordable water. With continuous economic development and increasing global population, surface water, groundwater, and even drinking water have been seriously affected by pollution [1,2]. Natural organic compounds (NOCs) and anthropogenic organic compounds (AOCs) are substances typically found in water bodies and harm the water quality. For instance, the natural presence of geosmin and isoborneol produced by cyanobacteria in water intended for human consumption can lead to an unpleasant taste and odor even at concentrations of a few ng L^{-1} [3,4]. However, compared to NOCs, most organic pollutants in water come from anthropogenic domestic, industrial, and agricultural activities [2,5].

It is widely recognized that agriculture has a detrimental impact on natural aquatic resources due to the use of pesticides and chemical fertilizers [1]. Furthermore, diverse phenolic, halogenated, and aromatic contaminants in water come from effluents produced by various industrial processes [2]. Discharging domestic sewage effluents into water bodies is another significant source of organic contaminants, including the so-called emerging pollutants released from personal care products and pharmaceuticals [6]. Most AOCs are toxic and can lead to severe diseases such as cancer, deformity, and gene mutations [7]. To make matters worse, many of these compounds are non-biodegradable and persist in water for long periods due to their stable structure, bringing risks to aquatic life and human health [8].

In 2020, over 2 billion people worldwide lacked access to safe drinking water, and more than twice that number lacked access to proper sanitation [9]. According to a Global Burden of Disease study, 1.2 million people died in 2017 due to unsafe water. To put this into context, this was three times the number of global deaths by homicides and the same number of global deaths in road accidents that year [10]. It should be mentioned that even populations with access to sanitation services are susceptible to the adverse effects of these pollutants, as conventional drinking water and urban wastewater treatment plants cannot effectively remove recalcitrant organic compounds from water [11]. The

inadequate management of domestic, industrial, and agricultural wastewater means that the water consumed by hundreds of millions of people is dangerously contaminated or chemically polluted. Therefore, there is an urgent need to develop an effective method for removing AOCs from wastewater.

Over the past few years, advanced oxidation processes (AOP) based on peroxymonosulfate (HSO_5^- , PMS), which can generate sulfate radicals ($\text{SO}_4^{\bullet-}$) that are capable of degrading AOCs into small molecules and carbon dioxide, have been among the most investigated methods for wastewater treatment [12]. Compared to traditional hydroxyl radical-based AOP (HO^\bullet , redox potential of 1.8-2.7 V and half-life of 20 ns), $\text{SO}_4^{\bullet-}$ can present similar or even higher redox potential (2.5-3.1 V), together with a longer half-life (30-40 μs) [13], in a wider working pH range (3-9) [14]. In addition, PMS is inexpensive, easy to transport and store, and has an asymmetric structure that can facilitate its activation compared to hydrogen peroxide (H_2O_2) [15]. However, PMS-AOP still face the disadvantages of high-energy consumption and poor activation performance [16].

Recently, photocatalyst-activated PMS technology has attracted the attention of numerous researchers due to its advantages of environmental friendliness, low energy consumption, and high degradation efficiency [12]. Regarding the heterogeneous system photocatalyst/PMS/light, on the one hand, photocatalysts can produce electrons and holes under the presence of light, which can effectively activate PMS to generate more oxidizing species. On the other hand, PMS can capture electrons; thus, the recombination of photogenerated carriers (e^-/h^+) can decrease, which can improve the catalytic performance of the photocatalysts [12]. In this sense, exploring photocatalysts that can activate PMS under visible light to produce active species capable of degrading organic pollutants is considered an essential step in the field of wastewater treatment. Moreover, it is also desirable that the photocatalyst can be recoverable, reusable, and environmentally sustainable [17].

Considering this, the aim of this thesis work was to develop PMS-assisted photocatalytic systems that could fulfill the aforementioned requirements and efficiently degrade organic pollutants. Therefore, the strategies used in this study were firstly to synthesize cobalt oxide (Co_3O_4), followed by the fabrication of Co_3O_4 coatings, which were employed to degrade pesticides in a continuous flow-cell reactor under simulated solar irradiation. Cobalt-based materials such as Co_3O_4 have drawn attention because cobalt ion (Co^{2+}) is considered the best activator of PMS [18]. Although Co_3O_4 had been

applied for the photocatalytic activation of PMS before [19], herein its performance was studied in a continuous flow reactor for the first time.

Secondly, the $g\text{-C}_3\text{N}_4/\text{NiFe}_2\text{O}_4$ photocatalyst was synthesized and evaluated regarding its ability to activate PMS for the degradation of antibiotics under visible light in a batch system. Although carbon nitride ($g\text{-C}_3\text{N}_4$) has outstanding properties (high stability, competitive cost, easy fabrication, and narrow band gap), its high electron-hole pair recombination rate, low ability to utilize visible light, and difficulty in separating it from aqueous media have limited its application in PMS-AOP [20,21]. The hypothesis adopted here was that the coupling between the two semiconductors would enhance the performance of $g\text{-C}_3\text{N}_4$ in activating PMS due to the formation of a heterojunction. Nickel ferrite was chosen for this purpose not only because it has a suitable band position that matches well with that of $g\text{-C}_3\text{N}_4$ to promote an effective separation of the photogenerated charges but also because it possesses a narrow band gap energy and excellent magnetic properties, which could extend the response of the photocatalyst to visible light and facilitate its recovery for reuse [22]. Additionally, no studies have explored the potential of the photocatalytic activation of PMS by $g\text{-C}_3\text{N}_4/\text{NiFe}_2\text{O}_4$ and its application for the degradation of organic compounds.

1.2. Literature Review

1.2.1. Peroxymonosulfate-based advanced oxidation processes (PMS-AOP)

Advanced oxidation processes comprise a series of technologies that involve the generation of highly oxidizing species capable of degrading refractory organic compounds into less toxic substances or even mineralizing them into carbon dioxide and water [23]. Figure 1.1 shows a simplified diagram depicting the different types of AOP.

For many years, most AOP were based on the generation of hydroxyl radicals as active species for the degradation of organic compounds [24]. However, as shown in Figure 1.2, peroxymonosulfate-based AOP emerged in the last few years and currently is considered a research hotspot due to their unique properties and advantages.

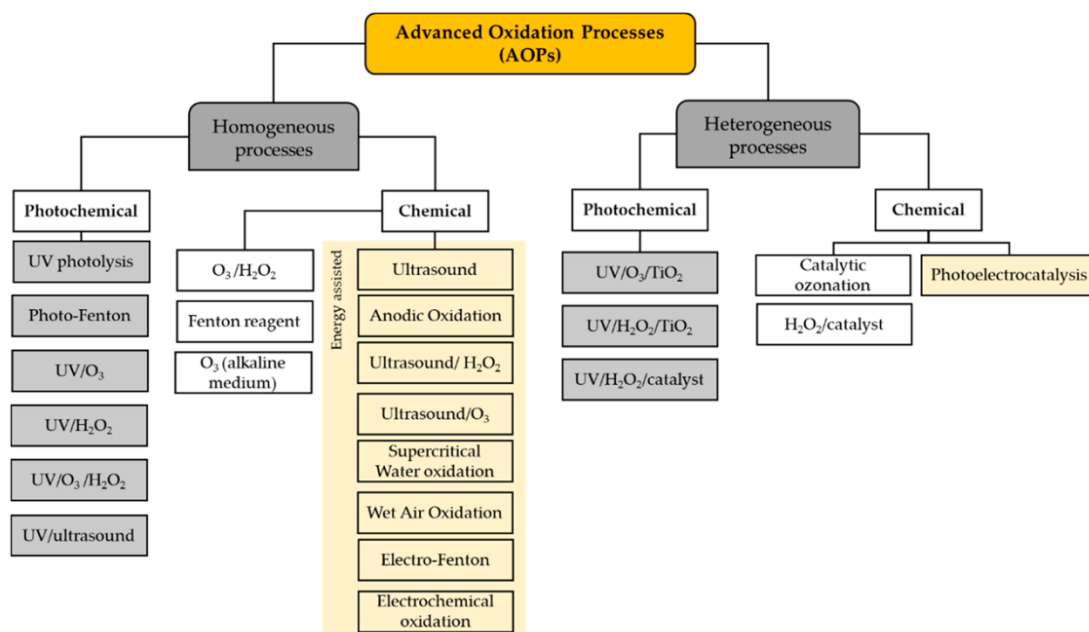


Figure 1.1. Different types of AOP that have been used for the degradation of organic pollutants. Adapted from [25].

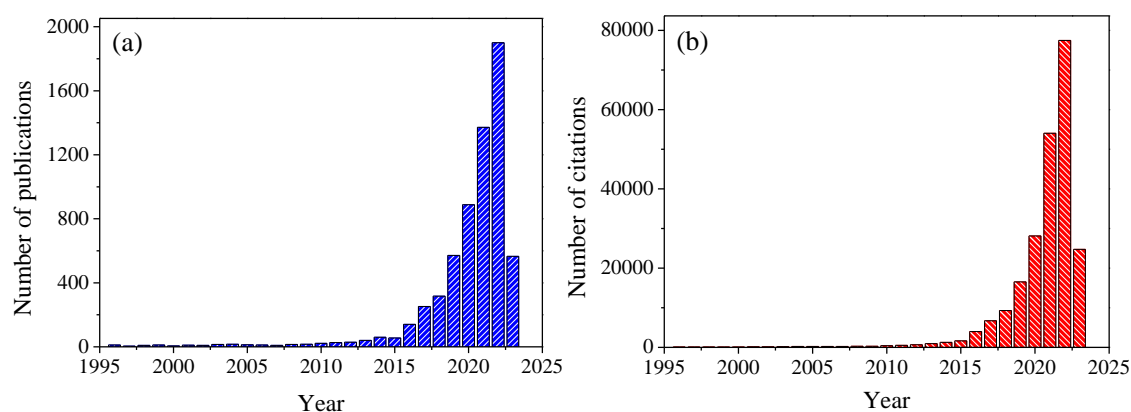


Figure 1.2. Number of publications (a) and citations (b) per year since 1996 based on the search for “peroxymonosulfate” in the Web of Science (Access in June 2023).

In PMS-AOP, peroxymonosulfate can be activated to generate sulfate radicals which, compared to HO^\bullet , have a higher redox potential (HO^\bullet : 1.8-2.7 V; $\text{SO}_4^{\bullet-}$: 2.5-3.1 V), longer half-life (HO^\bullet : 20 ns; $\text{SO}_4^{\bullet-}$: 30-40 μs) [26], higher selectivity, and reduced sensitivity to pH variations [14]. Basically, peroxymonosulfate is a derivative of hydrogen peroxide with an asymmetric structure in which an SO_3 group replaces an H atom in H_2O_2 [13]. The peroxide bond (O-O) distances in H_2O_2 and PMS are 1.453 Å and 1.460 Å, respectively. Therefore, since the O-O bond length of PMS is longer than the O-O bond length of H_2O_2 , it requires less energy to break it, thus facilitating the PMS

activation compared to H_2O_2 [27]. The precursor of PMS is a triple salt of potassium ($\text{KHSO}_5 \cdot 0.5\text{KHSO}_4 \cdot 0.5\text{K}_2\text{SO}_4$), commercially known as Oxone. In addition to being very stable, inexpensive, non-toxic, and highly soluble in water ($> 250 \text{ g L}^{-1}$ at $20 \text{ }^\circ\text{C}$), it is easier to transport and store than the aqueous H_2O_2 [13]. Some of the specific characteristics of PMS are listed in Table 1.1.

Table 1.1. Characteristics of PMS [13].

Peroxymonosulfate ion	Properties
Structure	$\begin{array}{c} \text{O} \\ \\ \text{O}^- - \text{S} - \text{O} - \text{O} - \text{H} \\ \\ \text{O} \end{array}$
Formula	HSO_5^-
Molecular weight	113.07 g L^{-1} (614.74 g L^{-1} Oxone)
Solubility in water	$> 250 \text{ g L}^{-1}$ at $20 \text{ }^\circ\text{C}$ (based on Oxone)
Redox potential	1.82 V
Other names	Caroat, monopersulfate, Oxone, Curex

Although PMS is a strong oxidant, its direct reaction with most pollutants is slow, so its activation is required. The two most common routes for activating PMS to generate $\text{SO}_4^{\bullet-}$ species involve breaking the peroxy (O-O) bond in its structure using either external energy or transferred electrons. Energy-based activation can be achieved using ultraviolet irradiation, heat, or ultrasound, according to Equations 1.1-1.3, whereas, the electron-transfer-based activation occurs through transition metal ($\text{M} = \text{Mn}^{2+}, \text{Fe}^{2+}, \text{Co}^{2+}, \text{Ni}^{2+}$) catalytic-based reactions (Equations 1.4 and 1.5) or photocatalytic reactions (Equation 1.6) [15]. These processes are illustrated in Figure 1.3.



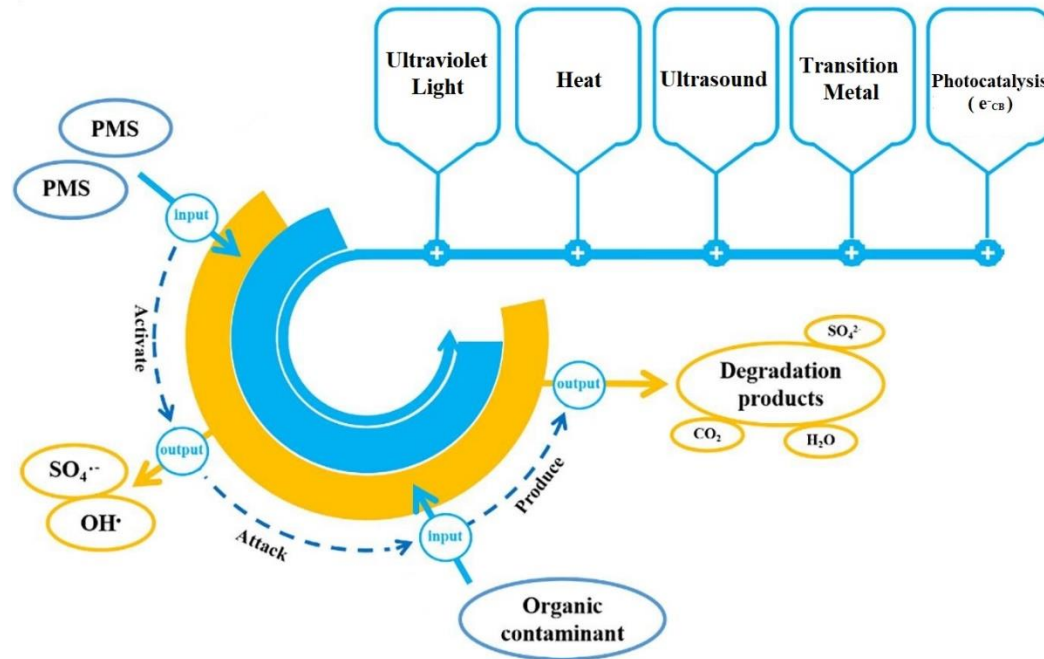
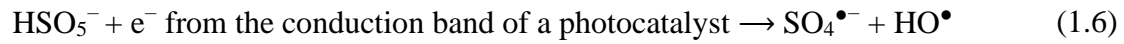


Figure 1.3. Different methods for activating PMS. Adapted from [27].

Although the processes illustrated in Figure 1.3 can activate PMS, they have some limitations, including:

- *PMS activation via external energy:* Ultrasound and heat-driven PMS activation require expensive reactors, which hinders their large-scale applicability [28]. Using ultraviolet light can result in significant energy consumption; therefore, PMS activation under milder conditions using visible light or sunlight is desirable [29].

- *PMS activation via transition-metal-based homogenous and heterogeneous catalysis:* Despite being considered more cost-effective and easy operation methods than the energy-based approaches, both homogeneous and heterogeneous catalysis face limitations. Regarding homogeneous systems, first, the recovery of dissolved metal ions is difficult and requires further separation steps. Second, the treatment of high organic concentration wastewater requires a large amount of metal ions, posing a secondary pollution risk. Third, the catalytic performance is highly affected by pH because transition metals can precipitate under alkaline conditions and form hydrated species under acidic

conditions. Fourth, organic compounds can be bonded to metal ions, which also affects PMS activation [26]. Compared to homogeneous systems, heterogeneous systems bring some advantages since the catalyst is solid, allowing its recovery and reuse, supporting a wider pH range, and minimizing the release of metal contaminants into the environment [30]. However, heterogeneous systems suffer from limited efficiency in activating peroxymonosulfate due to the slow $M^{(n+1)+}/M^{n+}$ regeneration cycle (Equations 1.4 and 1.5), which is considered the rate-limiting step in this process [31].

Fortunately, the photocatalytic activation of PMS can overcome the shortcomings mentioned above and shows promising application prospects owing to its high efficiency and potential for solar energy utilization.

1.2.2. Heterogeneous photocatalytic activation of PMS

In a typical photocatalytic process, the reaction is triggered when a semiconductor is illuminated with ultraviolet or visible light radiation and absorbs photons with energies equal to or higher than the energy of its band gap. Next, electrons (e^-) in the valence band (VB) of the semiconductor are excited to its conduction band (CB) with the simultaneous generation of holes (h^+) in the valence band. Then, the photogenerated carriers migrate to the catalyst surface, where the holes can oxidize the adsorbed water to produce hydroxyl radicals, while the electrons can reduce dissolved oxygen molecules to generate superoxide radicals (Equations 1.7 and 1.8) [32].



As an oxidant, PMS can be used as an electron acceptor in the photocatalytic process. So, when the photogenerated electrons are trapped by PMS, both hydroxyl and sulfate radicals can be generated (Equation 1.6). Therefore, the addition of PMS to the reaction media can enhance the separation of electron-hole pairs and improve the efficiency of the photocatalytic process by producing more reactive radicals to decompose organic compounds [15]. Figure 1.4 shows the mechanism of PMS activation via photogenerated electrons.

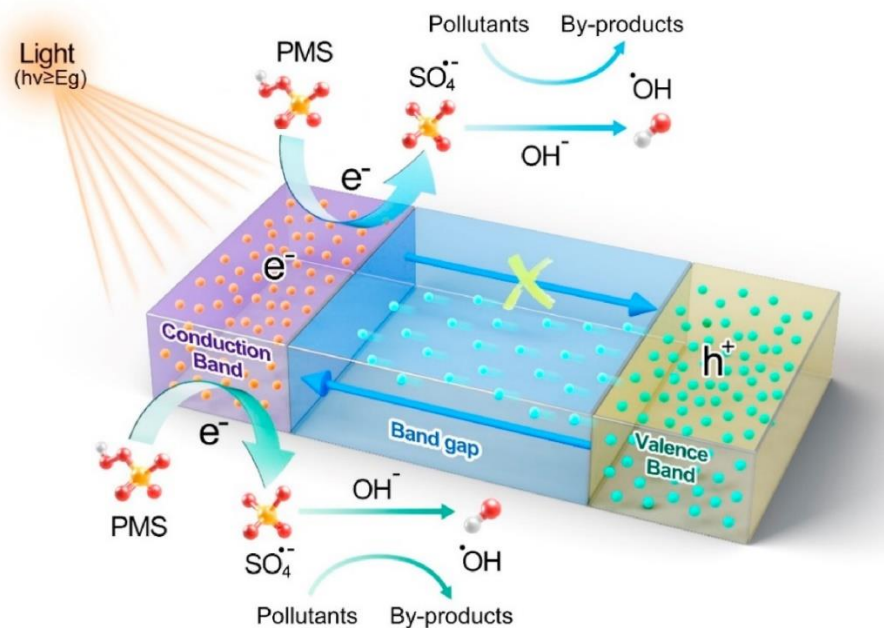


Figure 1.4. PMS activation by photogenerated electrons. Adapted from [15].

During the past few decades, titanium dioxide (TiO_2) was the first photocatalyst to stand out in the field of photocatalysis owing to its good performance, low cost, stability, and low toxicity. However, its utilization has been hampered by its large bandgap (3.2 eV), which requires ultraviolet light for activation. Because only approximately 5% of the solar spectrum consists of UV light, while visible light contributes 45% of it, a visible-light-driven photocatalyst is desirable for effective applications [21]. With unique optical, structural, and physicochemical properties, cobalt oxide and carbon nitride have been considered potential candidates for environmental and energy applications [18,20]. Considering this, many studies have focused on evaluating their performance in activating PMS to degrade organic pollutants under visible light.

1.2.2.1. Cobalt oxide (Co_3O_4)

In 2004, a pioneering study conducted by Anipsitakis et al. [33] revealed that the cobalt ion (Co^{2+}) is the most efficient transition metal for the activation of PMS. However, homogeneous catalytic reactions of the Co^{2+} /PMS system in aqueous solutions discharge cobalt ions into water, constituting a potential threat to human beings, in addition to increasing the operational cost due to cobalt loss [18]. To overcome the disadvantages of Co^{2+} /PMS homogeneous systems, heterogeneous cobalt catalysts, such as CoO , CoO_2 , Co_2O_3 , and Co_3O_4 have been investigated for PMS activation [18,26]. Among them,

Co_3O_4 has exhibited excellent performance due to the presence of Co^{2+} and Co^{3+} species in its structure, so its application to activate PMS for the degradation of organic pollutants in batch systems has been widely considered [26].

The PMS activation by Co_3O_4 nanoparticles was assessed by Anipsitakis et al. [33] for 2,4-dichlorophenol degradation, showing that the Co_3O_4 could efficiently activate PMS with low levels of cobalt leaching. Hu et al. [34] found that Co_3O_4 activated PMS system could efficiently degrade bisphenol A in water, while Chen et al. [35] successfully applied Co_3O_4 /PMS system for removing Acid Orange 7. Studies regarding Co_3O_4 nanoparticles immobilized on different supports, such as Raschig rings and polytetrafluoroethylene, were also conducted, presenting fast degradation rates of organic contaminants [36]. It was found that the immobilization of Co_3O_4 not only facilitates its separation and recovery after the reaction but also increases its stability, thereby reducing cobalt leaching [26]. Moreover, Co_3O_4 is not only an effective heterogeneous catalyst for PMS activation but is also a visible-light-driven photocatalyst. Taking this last property into account, Wang et al. [19] evaluated the Co_3O_4 performance for phenol degradation in the presence of PMS and solar irradiation, finding a synergistic effect between photocatalysis and PMS activation, which led to the generation of multiple active species. Overall, the highly efficient PMS activation and low level of cobalt leaching make Co_3O_4 a promising photocatalyst with reduced environmental risk.

1.2.2.2. Carbon nitride (g- C_3N_4)

The application of g- C_3N_4 as a visible-light-driven photocatalyst was first reported by Wang et al. [37] in 2009. Since then, g- C_3N_4 has been widely investigated in photocatalysis due to its competitive cost, easy fabrication, high stability, and narrow band gap (~ 2.7 eV). Because of all these outstanding properties, g- C_3N_4 could be considered an ideal material for activating PMS to remove organic pollutants under visible light. However, it has been reported that its performance in this process remains far from satisfactory due to the fast recombination of photogenerated e^-/h^+ pairs and weak visible light absorption [20]. Several approaches have been proposed to overcome these limitations, such as metal doping, morphology modification, noble metal deposition, and constructing heterojunctions. Among them, it was verified that the photocatalytic activity of g- C_3N_4 can be improved by coupling it with another semiconductor in order to form a heterojunction that decreases the recombination rate of the photogenerated charges, thus

improving the photoactivity. Assembling a heterojunction mainly requires the combination of band structures and the nearby contact between two or more semiconductors, so the photogenerated e^-/h^+ pairs can be quickly transferred across the interface for subsequent photoreactions.

Yue et al. [38] synthesized a $g\text{-C}_3\text{N}_4/\text{CoWO}_4$ type II heterojunction with remarkable photoactivity for the degradation of tetracycline hydrochloride in the presence of PMS and visible light. The authors found a better separation of the photogenerated charges in the composite material than in the pure phases, attributed to the charge transfer between the two semiconductors. The electrons in the CoWO_4 CB (-1.17 V) migrated to the $g\text{-C}_3\text{N}_4$ CB (-1.05 V), while the holes in the $g\text{-C}_3\text{N}_4$ VB (+1.88 V) moved to the CoWO_4 VB (+1.23 V), thus providing a higher electron lifetime, which was beneficial for activating PMS. Moreover, the Co from CoWO_4 also reacted with PMS and accelerated its decomposition to generate more radicals. Other examples of heterostructures that exhibited better performance than the isolated materials for PMS photoactivation for the removal of organic pollutants include $g\text{-C}_3\text{N}_4/\text{CuO}$ [39], $g\text{-C}_3\text{N}_4/\text{ZIF-NC}$ [40], $\text{MoO}_3/\text{Bi}_2\text{O}_3/g\text{-C}_3\text{N}_4$ [41], $g\text{-C}_3\text{N}_4/\text{FeWO}_4$ [42], $g\text{-C}_3\text{N}_4/\text{NiCo}_2\text{O}_4$ [43].

Despite the progress achieved and reported in these studies, the recovery of most of these materials remains an important challenge because powder catalysts are often difficult to separate from the aqueous phase, which can cause material loss and secondary pollution, thus limiting their practical application [12]. One of the most promising methods to overcome this drawback is the use of magnetic photocatalysts. Recently, metal ferrites, with the general formula MFe_2O_4 ($\text{M} = \text{Co}, \text{Cu}, \text{Mn}, \text{Zn}$), have received wide attention due to their abundant sources, strong stability, narrow band gap, and outstanding ferromagnetism, which allow them to be easily recovered from the aqueous medium by the application of an external magnetic field [44]. Taking this into account, it has been considered a promising strategy to combine $g\text{-C}_3\text{N}_4$ with metal ferrites to assemble a magnetic heterojunction for the remediation of environmental organic pollution. Inspired by these ideas, Li et al. [45] designed a ternary magnetic $g\text{-C}_3\text{N}_4/\text{BiVO}_4/\text{CuFe}_2\text{O}_4$ heterojunction with superior performance for levofloxacin degradation in a PMS-assisted photocatalytic process. Due to its magnetic properties, the composite was easily recovered from the aqueous solution using a magnet and used in four additional cycles. Sarkar et al. [46] synthesized a magnetic $g\text{-C}_3\text{N}_4/\text{CoFe}_2\text{O}_4$ composite and applied it to degrade a textile effluent containing reactive dyes (RD) through the combination of peroxymonosulfate and photocatalysis. The photocatalytic studies demonstrated a 99%

removal and a degradation efficiency above 86% was maintained after three reuse cycles. Similar to these works, various other magnetic g-C₃N₄-based heterojunctions, such as g-C₃N₄/NiFe₂O₄ [22], g-C₃N₄/ZnFe₂O₄ [47], g-C₃N₄/CuFe₂O₄ [48], g-C₃N₄/MnFe₂O₄ [49] were used to activate H₂O₂ for the degradation of organic pollutants under visible light.

1.3. Objectives and Thesis Outline

Considering the state of the art on photocatalyst-activated PMS technology and the aforementioned scenario, the aim of this work was to develop PMS-assisted visible-light-driven-photocatalytic systems for the degradation of organic compounds. To achieve this objective, two new approaches were studied with the following specific objectives:

- Evaluate the performance of Co₃O₄ to activate PMS for the degradation of the pesticide imidacloprid (IMD) in a continuous flow-cell reactor under simulated solar irradiation;
- Evaluate the performance of g-C₃N₄/NiFe₂O₄ to activate PMS for the degradation of a simulated wastewater containing the antibiotic tetracycline hydrochloride (TCH) in a batch system under visible light.

The results are presented in two chapters. In Chapter 2, Co₃O₄ was synthesized, characterized, and immobilized in the form of films used to photoactivate PMS for IMD degradation in a flow-through reactor. A detailed study on how the concentration of PMS, flow rate, and type of radiation (visible and solar) affect the photocatalytic performance of the system was conducted. Additionally, quenching experiments were performed to investigate which oxidizing species are responsible for IMD degradation in Co₃O₄/PMS/solar irradiation process, along with analyses to detect reaction byproducts. Based on these results, the reaction mechanism and the degradation pathway of imidacloprid were elucidated.

In Chapter 3, g-C₃N₄, NiFe₂O₄, and g-C₃N₄/NiFe₂O₄ photocatalysts were synthesized, characterized, and evaluated regarding their ability to activate PMS for TCH degradation under visible light. In order to evaluate the performance of the g-C₃N₄/NiFe₂O₄ composite for use in more practical applications, photocatalytic tests were conducted at different initial pH values and in the presence of various typical

anions (Cl^- , SO_4^{2-} , NO_3^- , and HCO_3^-) commonly found in wastewaters. In addition, the stability of the composite was investigated through cyclic degradation tests. Finally, using quenching assays, the active species responsible for TCH degradation were identified, and the degradation mechanism of TCH in the g- $\text{C}_3\text{N}_4/\text{NiFe}_2\text{O}_4/\text{PMS}$ /visible light system was unveiled.

In Chapter 4, an overall conclusion about the main results obtained in this thesis is presented, along with suggestions for future works.

CHAPTER 2

PEROXYMONOSULFATE ACTIVATION BY Co_3O_4 COATINGS FOR IMIDACLOPRID DEGRADATION IN A CONTINUOUS FLOW-CELL REACTOR UNDER SIMULATED SOLAR IRRADIATION

2.1. Introduction

Imidacloprid, 1-(6-chloro-3-pyridylmethyl)-N-nitroimidazolidin-2-ylideneamine, is a neonicotinoid pesticide commonly used for the control of insect pests such as aphids, fleas, termites, whiteflies, turf and soil insects, and some beetles [50]. The main uses of IMD include agricultural, veterinary, and domestic applications [51]. Due to its broad-spectrum characteristics, high insecticidal activity, and long-term effectiveness, imidacloprid became the largest selling insecticide and the second largest selling pesticide worldwide in 2008 [52]. However, the massive use of IMD in agricultural and urban areas, its low volatility and biodegradability, and high solubility and stability in water [51] create a potential risk of water contamination when it is transported to surface waters in runoff or is leached into groundwater after application [53]. Numerous monitoring studies conducted over the last few years have confirmed this concern, since IMD has been detected in surface waters at concentrations up to $320 \mu\text{g L}^{-1}$ [51,54–56]. At concentrations below $1.0 \mu\text{g L}^{-1}$, IMD has chronic effects on aquatic insects, while acute toxicity is reached at below $20 \mu\text{g L}^{-1}$ in nontarget organisms including *Hyaella azteca*, ostracods, and *Chironomus riparius* [57]. Moreover, IMD may cause severe sublethal effects in vertebrate animals (some mammals, birds, and fishes), such as reduced growth and reproductive rates, impaired nervous system and immune function, weakened mobility, disturbed metabolic balance, and DNA damage [53]. Despite its detectable concentrations in water bodies have been ranged from ng L^{-1} to $\mu\text{g L}^{-1}$, several previous works focused their studies on high concentrations ($3\text{--}40 \text{ mg L}^{-1}$) IMD removal, which was due to either analytical method limitations to accurately quantify very low concentration levels or the fact that IMD is currently not regulated by legislation in many countries [20,58–60].

Because of its persistent character, IMD cannot be efficiently removed using conventional techniques in municipal wastewater treatment plants. In this regard, advanced oxidation processes (AOP) based on sulfate radicals ($\text{SO}_4^{\bullet-}$) have recently

gained attention from the scientific community and have been investigated for the degradation of several organic compounds [61–63], including IMD [20]. The sulfate radical is a powerful oxidant that can be generated by scission of the peroxy bond of peroxymonosulfate (PMS, HSO_5^-) upon activation. Compared to traditional hydroxyl radical-based AOPs (redox potential of 1.8-2.7 V *vs.* NHE and half-life of 20 ns), $\text{SO}_4^{\bullet-}$ can present similar or even higher redox potential (2.5-3.1 V *vs.* NHE), together with a longer half-life (30-40 μs), in a wider working pH range (2-8) [13]. PMS can be activated by heat, ultrasound, ultraviolet irradiation, transition metals (homogeneous and heterogeneous), electrons of a semiconductor conduction band, or carbon catalysts [13]. Transition metals are usually preferred, due to their abundance and efficient activation of PMS to produce $\text{SO}_4^{\bullet-}$, resulting from their ability to transfer charge between different valence states [34]. Among them, the cobalt ion (Co^{2+}) is regarded the most effective [64]. However, its toxic nature causes secondary water pollution, which limits its practical application in homogeneous catalysis for water and wastewater treatment [65]. Therefore, it is necessary to use heterogeneous systems. To this end, cobalt-based catalysts such as Co_3O_4 have been investigated, in order to avoid Co^{2+} contamination while promoting PMS activation, as reported by Dionysiou et al. [33] for 2,4-dichlorophenol degradation using Co_3O_4 at neutral pH. The stability of Co_3O_4 was also reported by Chen et al. [35] and Hu et al. [34].

Co_3O_4 is not only an effective catalyst for PMS activation, but is also a visible light-driven photocatalyst. Therefore, when the $\text{Co}_3\text{O}_4/\text{PMS}$ system is illuminated with solar irradiation, the cobalt species in Co_3O_4 and the electrons in its conduction band can simultaneously activate PMS for the generation of sulfate radicals and other reactive oxygen species (ROS) [19]. Although the catalytic and photocatalytic activation of PMS by Co_3O_4 has already been investigated, only batch degradation has been considered until now. To the best of our knowledge, there are no reports concerning the performance of $\text{Co}_3\text{O}_4/\text{PMS}$ for the degradation of organic pollutants in a continuous system, employing an immobilized catalyst illuminated by solar irradiation. We believe that this is a promising strategy that can overcome the challenges associated with the use of suspended powder catalysts requiring laborious separation operations after the treatment.

In the present work, the photochemical activation of PMS by Co_3O_4 and solar light was investigated, for the first time, for the degradation of IMD in a continuous flow system. In order to achieve high degradation rates, the effects of PMS concentration, flow rate, and type of irradiation were investigated to determine the optimized operational

condition. The mechanism of IMD degradation in the $\text{Co}_3\text{O}_4/\text{PMS}/\text{solar}$ irradiation system was investigated using quenching experiments. Measurements by HPLC-high resolution mass spectrometry were used to identify the reaction intermediates and propose a degradation pathway.

2.2. Experimental

2.2.1. Reagents

Ammonium bicarbonate (NH_4HCO_3 , $\geq 99.5\%$), peroxymonosulfate (PMS, $\text{KHSO}_5 \cdot 0.5\text{KHSO}_4 \cdot 0.5\text{K}_2\text{SO}_4$, $\geq 95.0\%$) and sodium azide (NaN_3 , 99.0%) were purchased from Sigma-Aldrich. Cobalt (II) nitrate hexahydrate ($\text{Co}(\text{NO}_3)_2 \cdot 6\text{H}_2\text{O}$), methanol (MeOH , CH_3OH , HPLC grade), acetonitrile (CH_3CN , HPLC grade), tert-butyl alcohol (TBA, $\text{C}_4\text{H}_{10}\text{O}$, 99.0%), and p-benzoquinone (p-BQ, $\text{C}_6\text{H}_4\text{O}_2$, $> 99.5\%$) were supplied by Merck, Honeywell, Scharlau, Panreac, and Fluka Analytical, respectively. Technical grade imidacloprid (IMD, 97.9%) was obtained from Bayer Hispania S.A. (Barcelona, Spain). All chemicals were used as received.

2.2.2. Synthesis and characterization of Co_3O_4 nanoparticles

Co_3O_4 nanoparticles (NPs) were obtained by precipitation followed by calcination, similar to the synthesis described elsewhere [16]. Briefly, 1.81 g of $\text{Co}(\text{NO}_3)_2 \cdot 6\text{H}_2\text{O}$ was dissolved in a solution containing 70 mL of ethanol and 170 mL of ultrapure water, to which 1.49 g of NH_4HCO_3 was added, under stirring at room temperature. After 4 h, the purple precipitate formed was collected by centrifugation, washed with distilled water and ethanol, and dried overnight at 50 °C. The solid was calcined in air at 400 °C for 2 h, forming a black cobalt oxide powder.

The crystal structure of the Co_3O_4 was characterized by X-ray diffraction (XRD, PANalytical X'Pert Pro), using $\text{Cu K}\alpha$ radiation, and the crystallite size was estimated according to the Scherrer equation. Dynamic particle size and zeta potential (ζ -potential) measurements were performed by dynamic light scattering (DLS) at 25 °C, using a Malvern Zetasizer Nano ZS instrument. The textural structure of the catalyst was investigated by acquisition of N_2 adsorption-desorption isotherms at -196 °C, using a Micromeritics ASAP 2420 instrument, with the sample previously degassed overnight at 140 °C to a residual pressure of $<10^{-4}$ Pa. The specific surface area (S_{BET}) was determined

using the Brunauer-Emmett-Teller (BET) equation. The micropore volume and the external or non-microporous surface were analyzed by the t-method. The optical properties of the oxide were investigated by UV-Vis diffuse reflectance spectroscopy (DRS), using an Agilent Cary 5000 instrument.

2.2.3. Fabrication and characterization of Co₃O₄ coatings

The Co₃O₄ coating was produced by a simple vacuum filtration method. The Co₃O₄ powder (50 mg) was dispersed in 100 mL of ultrapure water and homogenized for 30 min using an ultrasonic processor (Bioblock Scientific). The suspension (10 mL) was vacuum filtered onto a glass microfiber filter (Whatman, 1 μm pore size, 47 mm diameter). The Co₃O₄ coating (0.4 mg cm⁻²) was dried overnight at 100 °C. The morphologies of the as-fabricated catalytic surfaces were observed by scanning electron microscopy (SEM, JEOL JSM-IT500 InTouchScope™), at an acceleration voltage of 15 kV, after coating the samples with gold.

2.2.4. Continuous degradation of imidacloprid in a flow-cell system

The continuous flow reaction was carried out at room temperature, using the experimental arrangement shown in Figure 2.1, which basically consisted of a reservoir containing the pesticide and PMS (1), a peristaltic pump (2), a bubble trap (3), a flow cell (7.7 cm³, Sigma-Aldrich) (4), a Xe arc lamp (5) (positioned 15 cm above the flow cell), and a reservoir for the treated solution (6). The cell was irradiated using a solar simulator equipped with a Xe lamp, herein referred to as “solar irradiation” (SI) (Heraeus TQ 150 Xe arc lamp, 18.2 W m⁻²). The same source was combined with a cut-off filter to remove the wavelengths lower than 400 nm, in order to restrict the operation only to the visible radiation region, herein denoted “visible irradiation” (VI) (Heraeus TQ Xe arc lamp with R3114 UV filter, < 3% transmission for light < 400 nm, 16.8 W m⁻²). The emission spectra and light source irradiance were measured with a StellarNet BLUE-Wave spectrometer and are displayed in Figures 2.2 and 2.3, respectively.

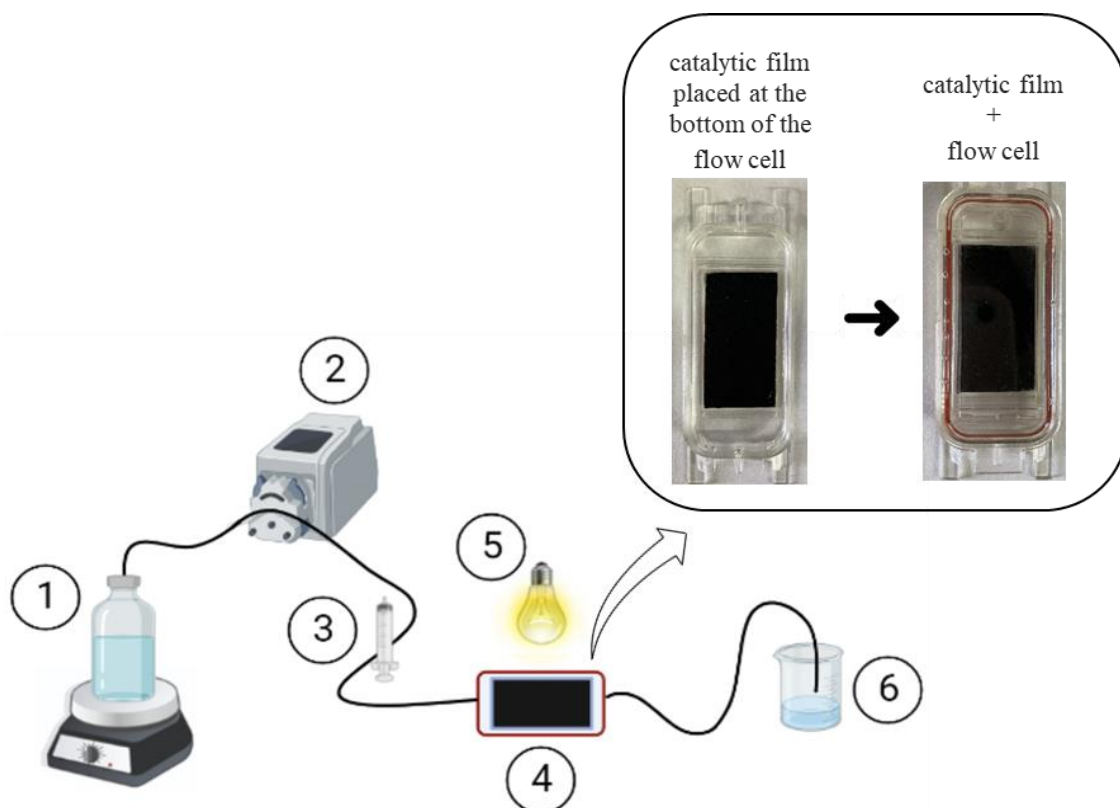


Figure 2.1. Schematic representation of the experimental arrangement used for IMD degradation: (1) reservoir containing the pesticide and PMS, (2) peristaltic pump, (3) bubble trap, (4) catalytic film + flow cell (7.7 cm³, Sigma-Aldrich), (5) Xe arc lamp (15 cm above the flow cell), and (6) reservoir for the treated solution.

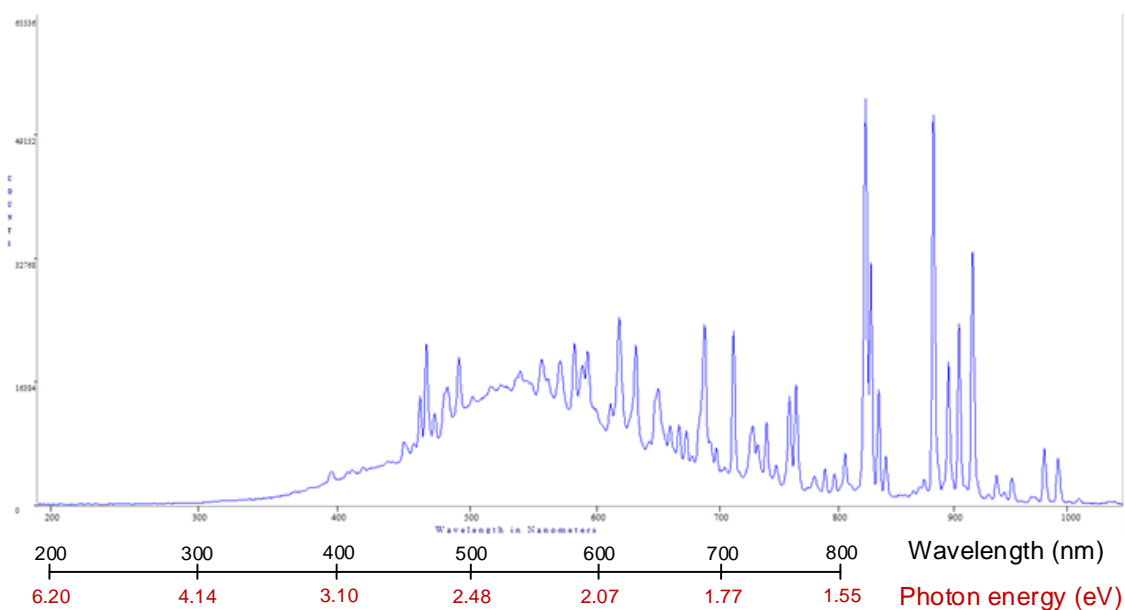


Figure 2.2. Emission spectra of the Heraeus TQ 150 Xe arc lamp.

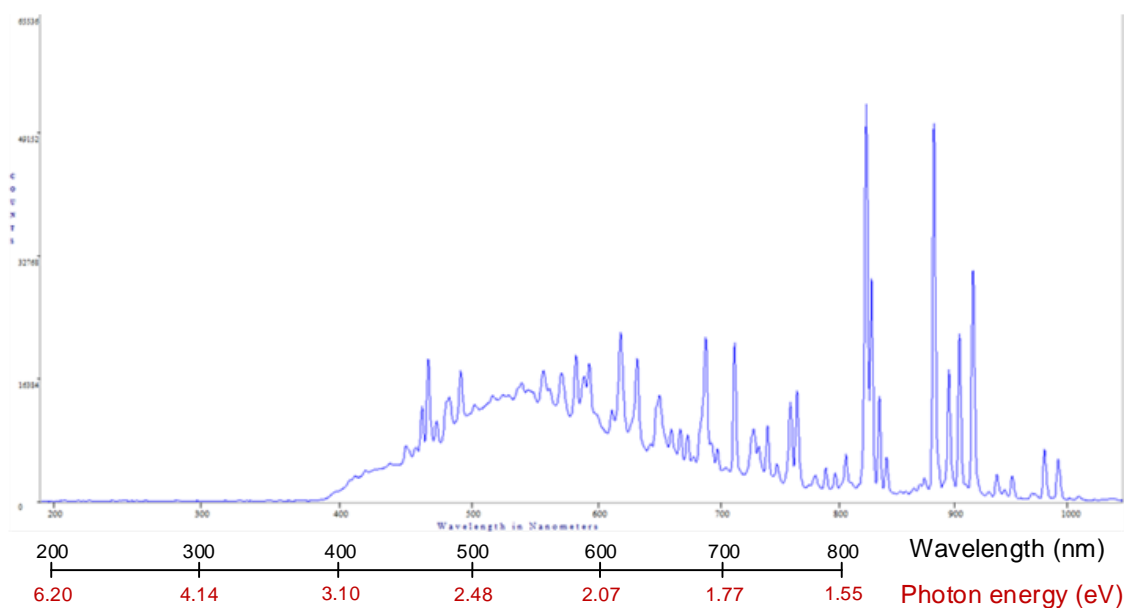


Figure 2.3. Emission spectra of the Heraeus TQ Xe arc lamp with R3114 UV filter.

Prior to the degradation assays, the Co_3O_4 coatings were washed with ultrapure water to remove any excess catalyst. After assembling the catalytic film (5.1 cm^2) and flow cell, the solution containing IMD (2.5 mg L^{-1}) and PMS (concentrations of 0.1, 0.2, or 0.4 g L^{-1}) was pumped through the reactor at a constant flow rate ($u = 0.10, 0.15,$ or 0.20 mL min^{-1}). Three different degradation approaches were studied: (i) catalytic activation of PMS (catalyst + PMS), (ii) heterogeneous photocatalysis (catalyst + irradiation), and (iii) photocatalytic activation of PMS (catalyst + PMS + irradiation). For the purpose of comparison, control assays were performed in the absence of the catalyst, applying the same experimental conditions. The experiments were performed for a maximum of 190 min, established considering the time necessary to reach steady-state, with samples being withdrawn from the reactor at predetermined time intervals. Prior to analysis of the IMD concentration, the samples were filtered using $0.2 \mu\text{m}$ pore size PVDF membranes and were immediately quenched with excess of methanol. In order to evaluate possible adsorption effects, a solution containing only IMD was fed continuously into the reactor during 1 h, under dark conditions, before starting the oxidation reaction.

Quenching experiments were also carried out to elucidate the main active species involved in the IMD degradation. Accordingly, 1 mM of CH_3OH , $\text{C}_4\text{H}_{10}\text{O}$, $\text{C}_6\text{H}_4\text{O}_2$, or NaN_3 was added to the IMD and PMS solution to scavenge sulfate, hydroxyl, superoxide, and singlet oxygen species, respectively [66].

2.2.5. Analytical procedures

The IMD concentration was measured by high-performance liquid chromatography (HPLC), using an Agilent LC 1260 system fitted with a diode array detector and a C18 ODS HYPERSIL column (5 μm , 150 \times 4.6 mm; Thermo Scientific). The analyses were performed at room temperature, employing a mobile phase consisting of 80% ultrapure water and 20% acetonitrile, at a flow rate of 1.0 mL min⁻¹. The detection wavelength was 270 nm. The intermediate compounds formed from the IMD degradation were identified by HPLC-high resolution mass spectrometry (HRMS), using a Bruker maXis II Q-TOF instrument (electrospray ionization mode). A reversed-phase C18 Zorbax-Extend column (5 μm , 150 mm \times 4.6 mm) was used for chromatographic separation, with a mobile phase composed of ultrapure water (79.9%), formic acid (0.1%), and acetonitrile (20%), at a flow rate of 0.8 mL min⁻¹. The concentration of total organic carbon (TOC) was determined using a Shimadzu TOC-VCSH system equipped with an ASI-V autosampler. The cobalt concentration was measured in aliquots of the treated solution by inductively coupled plasma optical emission spectroscopy (ICP-OES) (Varian-Agilent 720 with SPS3 injector), in order to determine whether cobalt had been leached from the catalyst during the experiments.

2.3. Results and discussion

2.3.1. Co₃O₄ characterizations

Figure 2.4 shows the X-ray diffractogram of the as-synthesized Co₃O₄. The material exhibited eight characteristic diffraction peaks, at 2θ of 18.94°, 31.17°, 36.72°, 38.42°, 44.66°, 55.46°, 59.15°, and 65.00°, corresponding to the (111), (220), (311), (222), (400), (422), (511), and (440) planes, respectively, of the cubic phase of Co₃O₄, according to the ICDS file (01-080-1542, space group Fd3m). Additional phases or impurities were not detected, consistent with the formation of a pure material. The crystallite size of the Co₃O₄ was 17 nm, according to the Scherrer equation, while the average particle size was 179.5 \pm 6.2 nm, determined from DLS measurements. Compared to the value obtained from XRD data, the particle size estimated by DLS was significantly higher, due to agglomeration/aggregation of primary particles in the suspension [67]. The Co₃O₄ nanoparticles were positively charged, exhibiting a ζ -potential of 35.0 \pm 0.5 mV at the natural suspension pH (6.86 \pm 0.06).

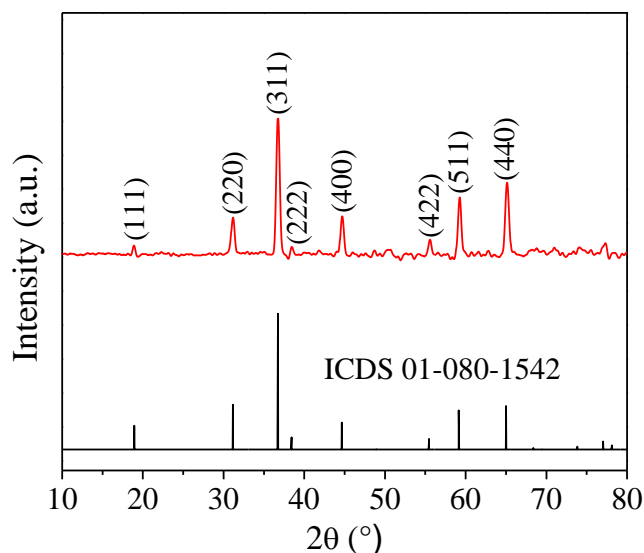


Figure 2.4. XRD pattern of the as-prepared Co_3O_4 nanoparticles.

According to the Brunauer-Deming-Deming-Teller (BDDT) classification, the type II N_2 adsorption-desorption isotherm for Co_3O_4 (Figure 2.5(a)) is commonly ascribed to non-porous, low porosity, or macroporous materials [68]. The BET specific surface area determined from the isotherm was $41.8 \text{ m}^2 \text{ g}^{-1}$. The H3 hysteresis is usually related to mesoporosity, with the observed isotherm loop being characteristic of materials with aggregates of plate-like particles, giving rise to slit-shaped pores [69]. The textural properties of the catalyst are summarized in Table 2.1, while the cumulative pore volume and pore size distributions are shown in Figure 2.5(b-c). It was found that the textural properties were governed by mesoporosity (59.3%) and macroporosity (40.7%) resulting from particle agglomerates, aggregates, or inter-particle spaces [68]. The Co_3O_4 presented a trimodal pore distribution in the range of mesopores (Figures 2.5(b-c)), with pore sizes of around 2.4, 23.6, and 43.6 nm.

Table 2.1. Summary of the textural properties of the Co_3O_4 .

Catalyst	S_{BET} ($\text{m}^2 \text{ g}^{-1}$)	A_{external} ($\text{m}^2 \text{ g}^{-1}$)	A_{micro} ($\text{m}^2 \text{ g}^{-1}$)	$V_{\text{micropores}}$ ($\text{cm}^3 \text{ g}^{-1}$)	$V_{\text{mesopores}}$ ($\text{cm}^3 \text{ g}^{-1}$)	$V_{\text{macropores}}$ ($\text{cm}^3 \text{ g}^{-1}$)	V_{total} ($\text{cm}^3 \text{ g}^{-1}$)
Co_3O_4	41.8	40.4	1.4	-	0.19	0.13	0.32

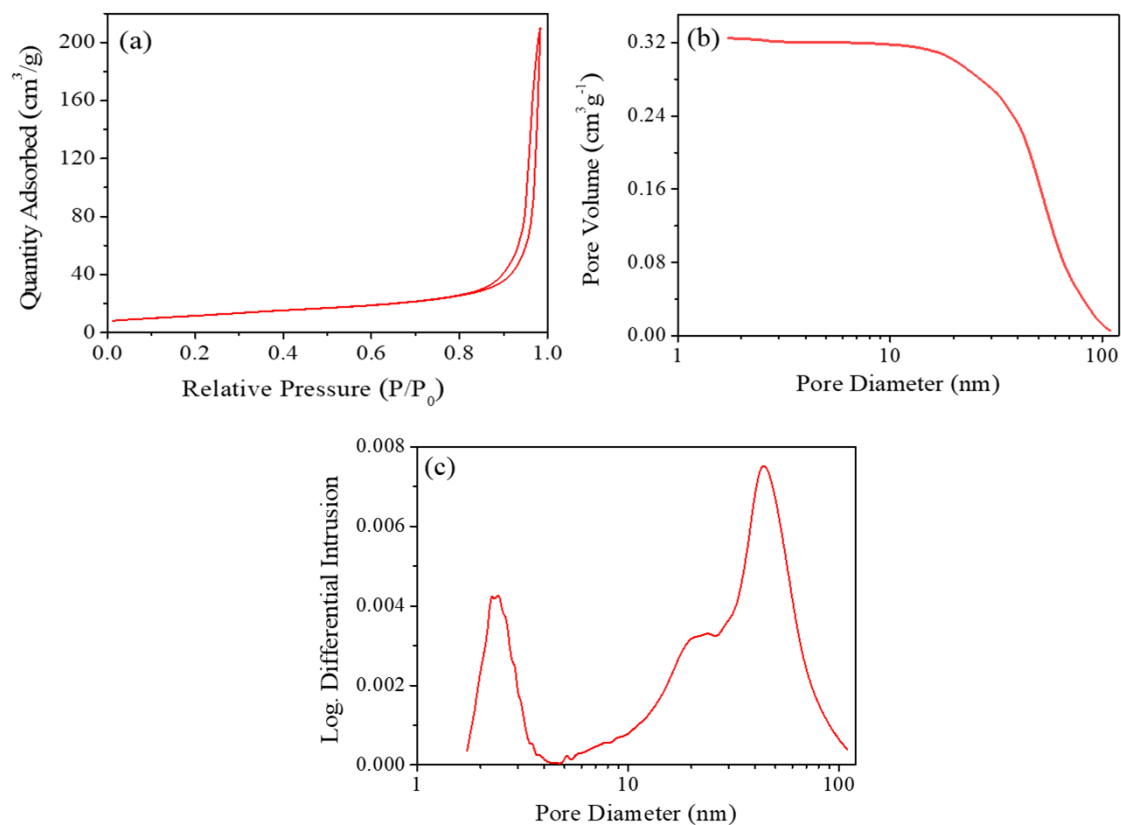


Figure 2.5. N₂ adsorption-desorption isotherm (a), cumulative pore volume (b) and pore size distributions (c) of the as-synthesized Co₃O₄ nanoparticles.

SEM images (top views) of the bare and Co₃O₄-coated glass microfiber filters are shown in Figure 2.6(a) and Figure 2.6(b-c), respectively. The Co₃O₄ NPs were successfully deposited as particle aggregates, at the submicron scale, and were evenly distributed over the glass microfiber surface. The presence of larger particles scattered on the surface was also observed.

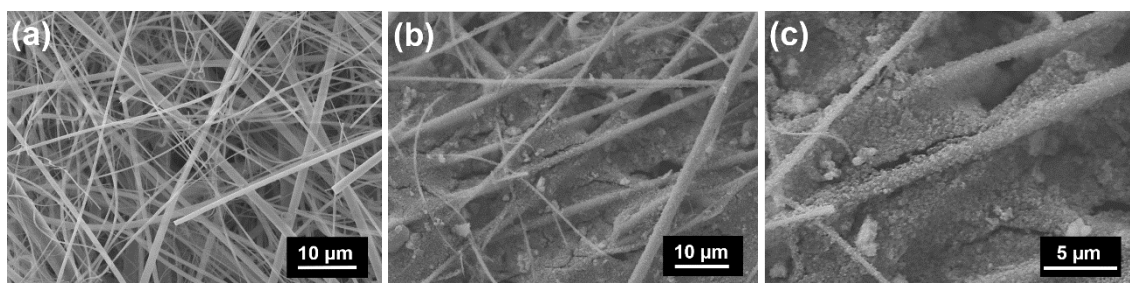


Figure 2.6. Top-view SEM images of the glass microfiber filter substrate (a) and the Co₃O₄-coated substrate fabricated by vacuum filtration (b-c).

The optical properties of the Co_3O_4 were evaluated from the UV-Vis absorption spectra (Figure 2.7(a)). Two absorption bands were observed in the ranges 300-550 nm and 600-800 nm, suggesting that the material could be activated by visible irradiation. The highest energy absorption band (E_{g1}) was attributed to charge transfer from O^{2-} to Co^{2+} (excitation from the optical band gap energy/valence to the conduction band) at the tetrahedral sites of the cubic lattice of Co_3O_4 . The less energetic absorption band (E_{g2}) was ascribed to charge transfer from O^{2-} to Co^{3+} (Co^{3+} level below the conduction band/sub-band located inside the energy gap) in the Co_3O_4 octahedral sites [70]. The direct band gap energies of Co_3O_4 were estimated using the Tauc method, by the interception of the tangent lines shown in Figure 2.7(b) with the abscissa of the plot of $(\alpha h\nu)^2$ against energy ($h\nu$) [70]. The band gap energies E_{g1} and E_{g2} were estimated as 2.12 eV and 1.56 eV, respectively, in good agreement with values reported in the literature [71].

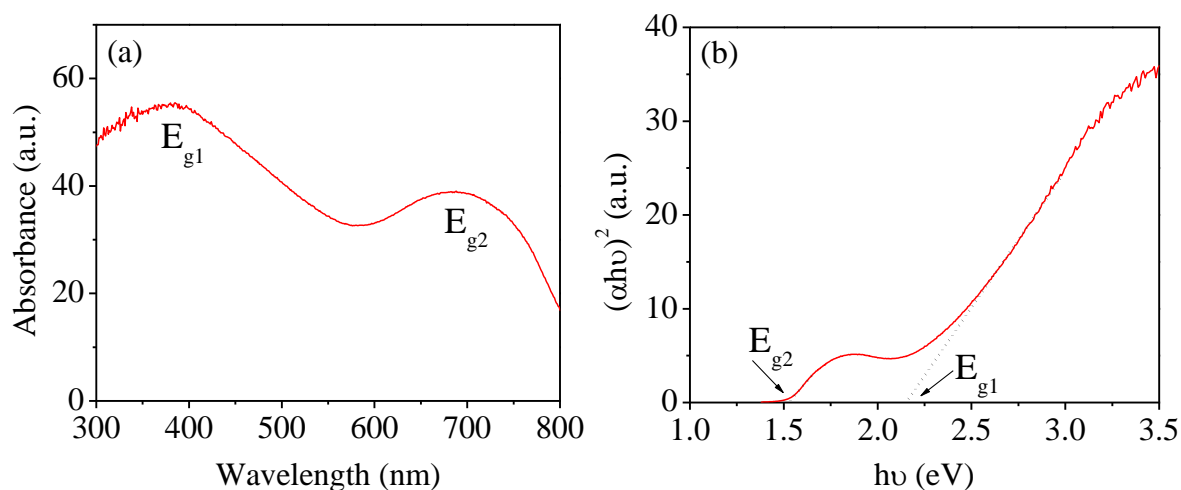


Figure 2.7. UV-Vis absorption spectrum (a) and Tauc plot (b) for the as-prepared Co_3O_4 nanoparticles.

2.3.2. Continuous degradation of IMD by Co_3O_4 in the presence of PMS and solar irradiation

The photochemical performance of the Co_3O_4 in the continuous-flow system, determined from the IMD degradation experiments, was expressed in terms of the normalized IMD concentration (C/C_0) according to reaction time, as shown in Figure 2.8 for different reaction conditions. In this figure, the negative values on the abscissa correspond to the time (1 h) during which the catalyst was in contact with the IMD

solution in the absence of PMS and irradiation, in order to identify possible adsorption effects. In this case, the pesticide uptake was less than 5%, demonstrating the low adsorption capacity of Co_3O_4 , which could be attributed to electrostatic repulsion, since both the Co_3O_4 surface (positive ζ) and the IMD molecules ($\text{pK}_a = 11.12$ [58]) were positively charged at the working pH. After allowing 60 min for adsorption, the IMD degradation process was started by providing PMS or/and light. As shown in Figure 2.8, the oxidation of IMD using PMS alone, photolysis, or photocatalysis was negligible from a practical point of view. In the case of the photocatalysis using Co_3O_4 , despite the optical properties shown in Figure 2.7(a), in the absence of PMS the photocatalytic activity was probably hindered by the fast recombination rate of the photogenerated electrons and holes [72] and the improper band edge positions. According to the Butler and Ginley relationship, the valence band (VB) and conduction band (CB) edge potentials of semiconductors at the point of zero charge can be calculated by Equations 2.1 and 2.2 [73,74]:

$$E_{\text{CB}} = E^{\circ} - X - 0.5E_{\text{g}} \quad (2.1)$$

$$E_{\text{VB}} = E_{\text{CB}} + E_{\text{g}} \quad (2.2)$$

where, E_{CB} and E_{VB} are CB and VB edge potentials; E° is the energy of free electrons on the hydrogen scale (~ 4.5 eV); X is the absolute electronegativity of the semiconductor (~ 5.903 for Co_3O_4); and E_{g} is the band gap energy of the semiconductor. Based on these equations, the CB and VB edge potentials values of Co_3O_4 were then determined to be 0.34 eV and 2.46 eV, respectively, which are in line with those reported by Long et al. [74]. As can be seen, the CB potential of Co_3O_4 (0.34 eV vs. NHE) is more positive than that of $\text{O}_2/\text{O}_2^{\bullet-}$ (-0.33 eV vs. NHE), indicating that the photogenerated electrons in the Co_3O_4 conduction band cannot reduce dissolve oxygen into $\text{O}_2^{\bullet-}$. Analogously, the VB potential of Co_3O_4 (2.46 eV vs. NHE) is more negative than that of $\text{H}_2\text{O}/\text{HO}^{\bullet}$ (2.72 eV vs. NHE), suggesting that photogenerated holes in the Co_3O_4 valence band cannot oxidize H_2O into HO^{\bullet} [75]. Conversely, there were significant effects of the synergies provided by solar irradiation + PMS and Co_3O_4 + PMS in the dark, with around 50% and 70% removal, respectively, reached after the transient time. In the first case, PMS could be activated by the UV component of the solar radiation, with the production of active species [76]. In the second case, PMS could be activated by Co^{2+} and Co^{3+} species in the

Co_3O_4 catalyst structure [16,77]. Interestingly, when the catalyst, PMS, and solar irradiation were combined, the IMD degradation increased further to 99%, evidencing the roles of different mechanisms contributing to the degradation process. Under this condition, 46% reduction of TOC was achieved at steady-state, indicating the formation of intermediate products. It should be noted that for all the experimental conditions, the average concentration of cobalt ions released into the solution was not higher than $33.3 \mu\text{g L}^{-1}$, which is far below the value allowed by the US EPA for drinking water ($100 \mu\text{g L}^{-1}$).

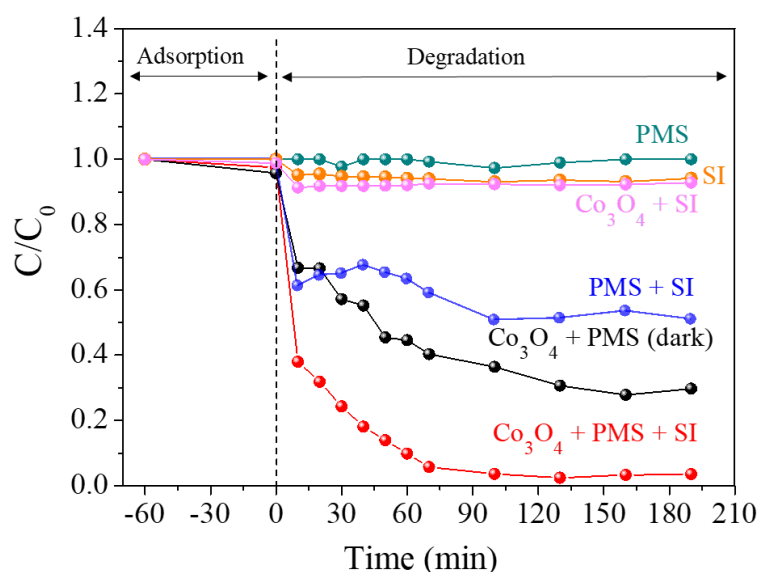


Figure 2.8. IMD degradation curves under different reaction conditions: —●— PMS only; —●— photolysis; —●— photocatalysis (in the absence of PMS); —●— PMS and SI; —●— Co_3O_4 and PMS in the dark; —●— Co_3O_4 and PMS under SI. Experimental conditions: $2.5 \text{ mg}_{\text{IMD}} \text{ L}^{-1}$; $0.4 \text{ mg}_{\text{catalyst}} \text{ cm}^{-2}$; $0.2 \text{ g}_{\text{PMS}} \text{ L}^{-1}$; $u = 0.1 \text{ mL min}^{-1}$.

Influence of operational parameters

Aiming to optimize the PMS-driven and photochemical effects, and to understand the performance of IMD degradation by Co_3O_4 , the effects of PMS concentration, flow rate, and type of irradiation were investigated. Figure 2.9 shows the IMD degradation using different PMS concentrations, in the dark and under solar irradiation. In the absence of light, there was a gradual increase of the IMD removal efficiency as the PMS concentration was increased from 0.1 to 0.4 g L^{-1} , due to the greater quantity of radicals produced. However, under solar irradiation, the removal efficiency remained almost constant (60%) when the PMS concentration was increased from 0.2 to 0.4 g L^{-1} . This

suggested that an excess of PMS could scavenge sulfate radicals (Equation 2.3) [78] or generate reactive species in such concentrations that they scavenged each other, before oxidizing the target pollutant (Equations 2.4-2.6) [19], consequently inhibiting further IMD degradation. In summary, the synergy achieved by integrating Co_3O_4 , PMS, and solar irradiation (Figure 2.9(b), solar irradiation) allowed the same removal efficiency observed in the absence of light (Figure 2.9(c), dark), but requiring half of the PMS content, thereby resulting in a more cost-effective and environmentally friendly process. Regarding the effect of flow rate (Figures 2.10(a-c)), higher conversion of IMD was achieved at a low flow rate (0.1 mL min^{-1}), due to the longer contact and residence time ($t = 77 \text{ min}$) of the fluid in the photoreactor.

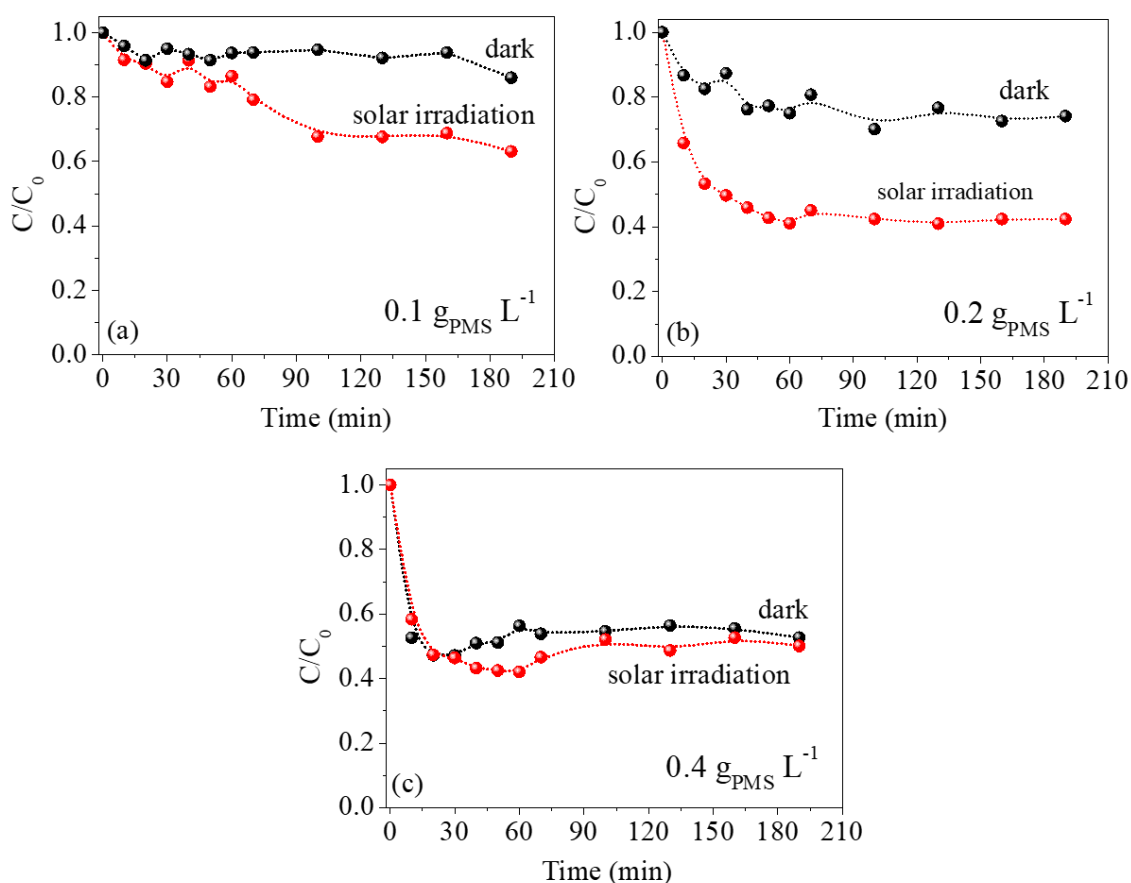


Figure 2.9. Effect of PMS concentration on IMD degradation under dark and solar irradiation. Experimental conditions: $2.5 \text{ mg}_{\text{IMD}} \text{ L}^{-1}$; $0.4 \text{ mg}_{\text{catalyst}} \text{ cm}^{-2}$; $u = 0.2 \text{ mL min}^{-1}$.



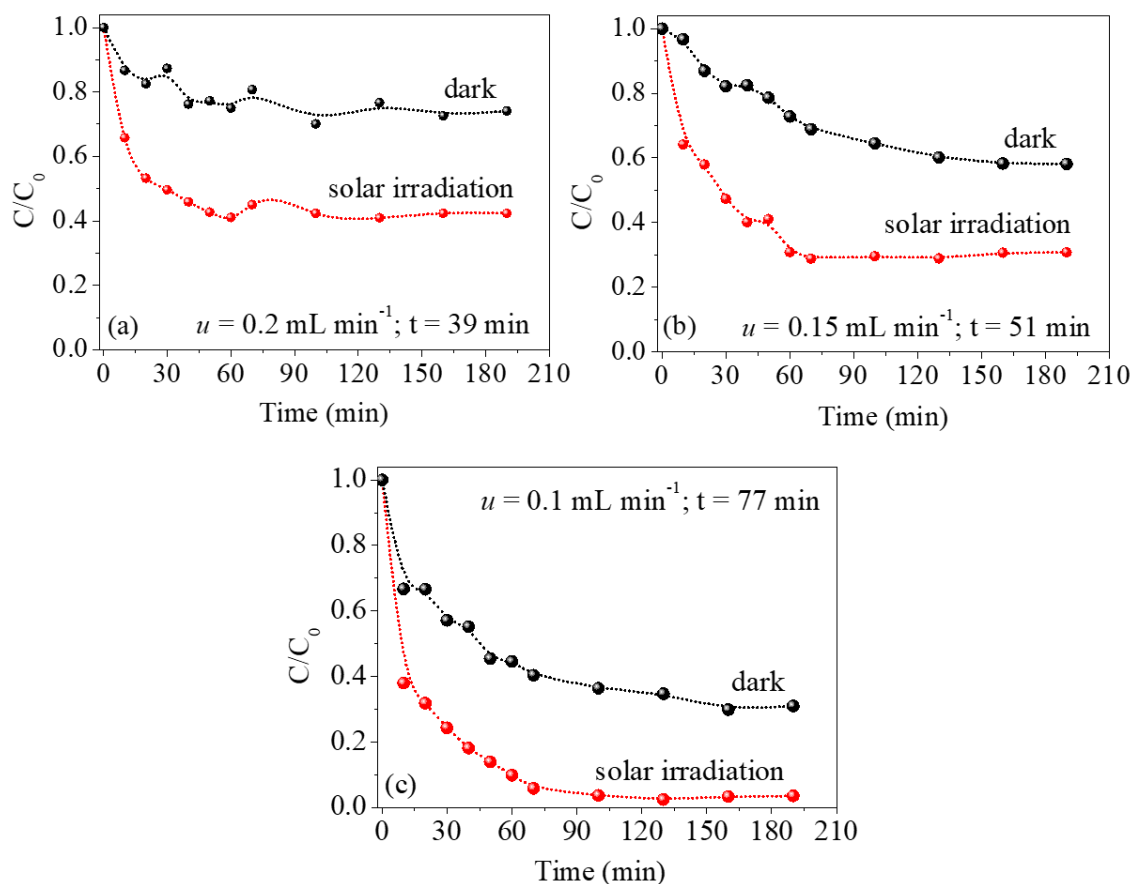


Figure 2.10. Effect of flow rate on IMD degradation under dark and solar irradiation. Experimental conditions: $2.5 \text{ mg}_{\text{IMD}} \text{ L}^{-1}$; $0.2 \text{ g}_{\text{PMS}} \text{ L}^{-1}$; $0.4 \text{ mg}_{\text{catalyst}} \text{ cm}^{-2}$.

The previous results enabled the establishment of the experimental conditions for further optimization of the process. In addition, in order to understand the effect of the type of irradiation on IMD degradation, an assay employing visible irradiation was carried out and the results were compared with those obtained under dark and solar irradiation conditions (Figure 2.11). Similar performances were observed for the processes in the dark and under visible irradiation, while significant improvement was achieved by exposure to solar irradiation. These results can be understood considering the band gap values of 2.12 eV (E_{g1}) and 1.56 eV (E_{g2}), corresponding to 585 nm and 794 nm, respectively, both present in the visible and solar radiation spectra (Figures 2.2 and 2.3). Considering that these wavelengths could photoactivate Co_3O_4 , improvements in IMD degradation would be expected, due to the PMS photocatalytic activation

mechanism. Therefore, absence of further IMD degradation using the $\text{Co}_3\text{O}_4/\text{PMS}/\text{VI}$ system indicated that the photocatalytic activation of PMS, involving conduction band electron transfer, did not play a significant role, under the experimental conditions used in this work. In contrast, the positive effects of the $\text{Co}_3\text{O}_4 + \text{PMS}$ and $\text{PMS} + \text{SI}$ combinations were clearly evident (Figure 2.8). This suggested that the improved degradation efficiency of the $\text{Co}_3\text{O}_4/\text{PMS}/\text{SI}$ system was mainly due to the activation of PMS by (i) Co^{2+} and Co^{3+} species in the Co_3O_4 catalyst structure, along with the UV component of solar radiation, either (ii) in the homogeneous phase or (iii) following the electrostatic adsorption of PMS onto Co_3O_4 . In the third case, the adsorption of negatively charged PMS anions on positively charged Co_3O_4 nanoparticles could weaken the bonds of PMS, facilitating and enhancing then its activation by UV irradiation. Liu et al. [79] and Mian and Liun [80] also reported the electrostatic adsorption of PMS by other catalysts.

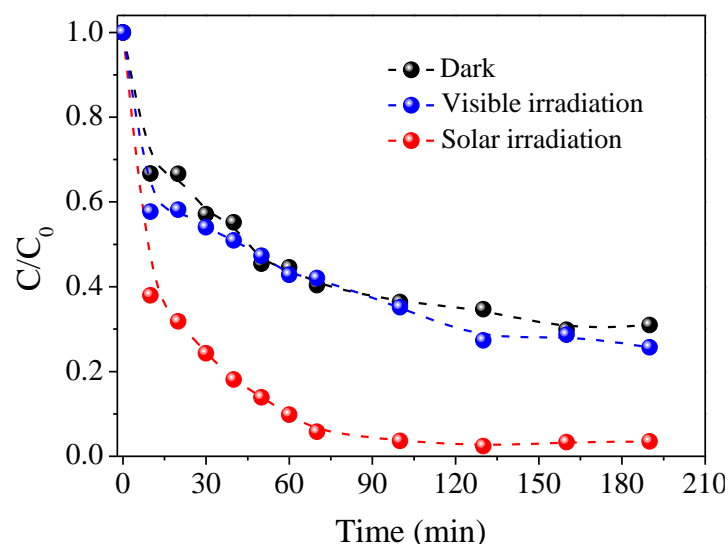


Figure 2.11. Effect of different irradiation types on IMD degradation. Experimental conditions: $2.5 \text{ mg}_{\text{IMD}} \text{ L}^{-1}$; $0.4 \text{ mg}_{\text{catalyst}} \text{ cm}^{-2}$; $0.2 \text{ g}_{\text{PMS}} \text{ L}^{-1}$; $u = 0.1 \text{ mL min}^{-1}$.

2.3.3. Mechanism of IMD degradation by $\text{Co}_3\text{O}_4/\text{PMS}/\text{solar}$ irradiation

In order to identify the main active species and propose the reaction mechanism for IMD degradation in the $\text{Co}_3\text{O}_4/\text{PMS}/\text{SI}$ system, quenching experiments were performed using methanol, tert-butyl alcohol, p-benzoquinone, and sodium azide as scavengers. MeOH is a trapping agent for the species HO^\bullet ($k = 9.7 \times 10^8 \text{ M}^{-1} \text{ s}^{-1}$) and $\text{SO}_4^{\bullet-}$ ($k = 2.5 \times 10^7 \text{ M}^{-1} \text{ s}^{-1}$) [77,81,82], while TBA is selective for HO^\bullet ($k = 3.8\text{-}7.6 \times$

$10^8 \text{ M}^{-1} \text{ s}^{-1}$) rather than $\text{SO}_4^{\bullet-}$ ($k = 4.0\text{-}9.5 \times 10^5 \text{ M}^{-1} \text{ s}^{-1}$) [34,77]. p-BQ is usually used to capture $\text{O}_2^{\bullet-}$ [66,77] and NaN_3 has a quenching effect on $^1\text{O}_2$ [66,79]. As shown in Figure 2.12, the addition of TBA had a negligible effect on IMD degradation, in comparison to the blank control, suggesting the minor role of hydroxyl species. Conversely, methanol addition led to significant inhibition, while dosing with p-BQ and NaN_3 resulted in complete inhibition. Considering the lower oxidation potential of $\text{O}_2^{\bullet-}$, compared to $^1\text{O}_2$ [77,82], the latter was probably the main species responsible for IMD degradation. In summary, it was demonstrated that $\text{SO}_4^{\bullet-}$, $\text{O}_2^{\bullet-}$, and $^1\text{O}_2$ were the reactive species associated with IMD removal in the $\text{Co}_3\text{O}_4/\text{PMS}/\text{SI}$ system. It is worth mentioning that the development of processes dominated by singlet oxygen, which is not usual in other AOPs, has been gaining attention for water treatment purposes, since recent studies have reported that $^1\text{O}_2$, rather than HO^{\bullet} and $\text{SO}_4^{\bullet-}$, is the main reactive species for degradation of organic pollutants [34,77,79], as well as for disinfection to eliminate microorganisms [82,83].

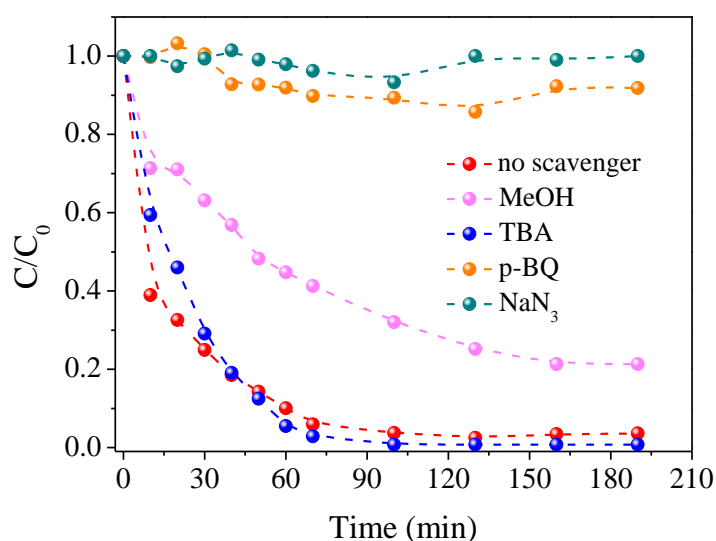
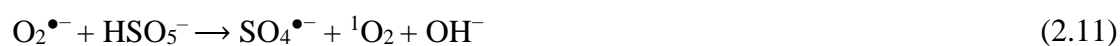
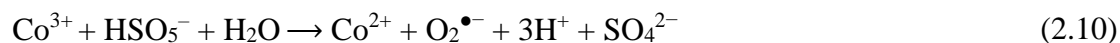
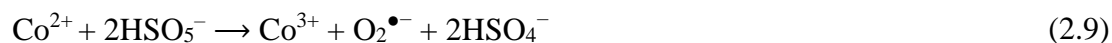
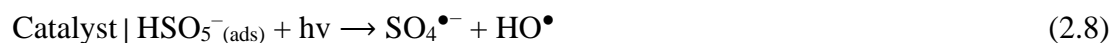


Figure 2.12. IMD degradation using the $\text{Co}_3\text{O}_4/\text{PMS}/\text{SI}$ approach in the presence of different radical scavenger species. Experimental conditions: $2.5 \text{ mg}_{\text{IMD}} \text{ L}^{-1}$; $0.4 \text{ mg}_{\text{catalyst}} \text{ cm}^{-2}$; $0.2 \text{ g}_{\text{PMS}} \text{ L}^{-1}$; $u = 0.1 \text{ mL min}^{-1}$. Scavenger concentration: 1 mM ; solar irradiation: 18.2 W m^{-2} .

Based on the results described above, a possible mechanism for IMD photodegradation was proposed. According to Equations 2.7 and 2.8, $\text{SO}_4^{\bullet-}$ and HO^{\bullet} radicals could be generated by means of the photoactivation of PMS by the UV component of solar radiation, either through direct photolysis of PMS in the aqueous

phase [19] or following its electrostatic adsorption onto Co_3O_4 surface, respectively. Due to the positive surface charge of the catalyst, Co_3O_4 might chemically adsorb HSO_5^- and weaken its bonds, facilitating then its photoactivation. Simultaneously, Co^{2+} and Co^{3+} could react chemically with PMS in a cyclic $\text{Co}^{3+}/\text{Co}^{2+}$ redox process, producing $\text{O}_2^{\bullet-}$ (Equations 2.9 and 2.10) [77,84]. Next, $\text{O}_2^{\bullet-}$ could give rise to $^1\text{O}_2$ upon oxidation (Equation 2.11) or recombination (Equation 2.12) [34,66]. Additionally, the produced HO^\bullet could further accelerate the PMS decomposition and generate $\text{SO}_5^{\bullet-}$ radicals (Equation 2.13) [85,86]. Then, the $\text{SO}_5^{\bullet-}$ radicals could react with each other to produce $\text{SO}_4^{\bullet-}$ via Equation 2.14 [85,86], and part of the $\text{SO}_4^{\bullet-}$ could be converted into $^1\text{O}_2$, according to Equation 2.15 [66]. Finally, $\text{SO}_4^{\bullet-}$, $\text{O}_2^{\bullet-}$, and $^1\text{O}_2$ could oxidize the IMD, converting it to intermediate compounds or eventually mineralizing it to carbon dioxide, water, and inorganic ions such as NO_2^- and Cl^- (Equation 2.16).



2.3.4. Pathway of IMD degradation by Co_3O_4 /PMS/solar irradiation

In addition to the IMD reaction mechanism, a degradation pathway was proposed from identification of the intermediate compounds found in the HRMS-HPLC analysis. Table 2.2 shows the main identified products, suggesting three possible degradation routes (R1, R2, and R3), displayed in Figure 2.13.

Table 2.2. IMD degradation intermediates in the Co₃O₄/PMS/SI process, detected by HRMS-HPLC.

Compound	Formula	Experimental mass (<i>m/z</i>)	Calculated mass (<i>m/z</i>)	Error (ppm)
IMD	C ₉ H ₁₀ ClN ₅ O ₂	255.0518	255.0517	0.1
I1	C ₉ H ₁₀ ClN ₅ O ₃	271.0467	271.0467	0.0
I2	C ₉ H ₈ ClN ₅ O ₃	269.0310	269.0312	-0.6
I3	C ₉ H ₁₀ ClN ₅ O ₄	287.0416	287.0419	-0.8
I4	C ₉ H ₁₁ ClN ₄ O ₂	242.0565	242.0566	-0.1
I5	C ₇ H ₉ ClN ₄	184.0511	184.0507	1.7
I6	C ₆ H ₄ ClNO ₂	156.9925	156.9923	1.8
I7	C ₂₄ H ₄₄ N ₄ O ₄	452.3357	452.3358	-0.1
I8	C ₃₆ H ₆₆ N ₆ O ₆	678.5033	678.5039	0.9

In route R1, the amidine nitrogen site of IMD can be attacked by the ¹O₂, yielding a nitrogen-centered radical cation, which upon the elimination of one hydrogen atom from the CH₂ units of the 5-member ring leads the formation of an α-aminoalkyl radical. Next, the α-aminoalkyl radical may quickly react with dissolved oxygen (DO) to produce the hydroxylated and carbonylated intermediates, I1 and I2 [87]. Further hydroxylation of I1 yields the product I3 [20]. Subsequently, I3 can be converted to I4 by loss of the nitro group (-NO₂). In the next steps, I4 can be further converted to I5 and then to 6-chloronicotinic acid (I6), or be directly converted to I6 [88]. Concurrently, in route R2, a similar reaction path as that observed for R1 takes place. However, the H-abstraction occurs in methylene bridge and the α-aminoalkyl radical reacts directly with DO and water to form I6 [87]. Subsequent degradation of I6 may eventually lead the cleavage of its aromatic ring yielding the formation of several short-linear molecules, including oxamic and oxalic acid, as a preceding step to complete mineralization to CO₂, H₂O and inorganic salts [89,90]. It is also worth noting that two high molecular weight products were detected (I7 and I8), which were probably oligomers of undetected dechlorinated fragments generated during the degradation process (route 3). Among the formed byproducts, the intermediates I1, I3 [91] and I4 [92] are considered to be less toxic for *Daphnia* and *Green Algae* than IMD by the ECOSAR analysis. In contrast, the predicted toxicity of 6-chloronicotinic for *Daphnia* and fish was found to be higher than that of the parent compound [93]. Therefore, future works need to conduct toxicity assessments in

order to ensure a better comprehension of the impact of intermediates in the $\text{Co}_3\text{O}_4/\text{PMS}/\text{SI}$ process.

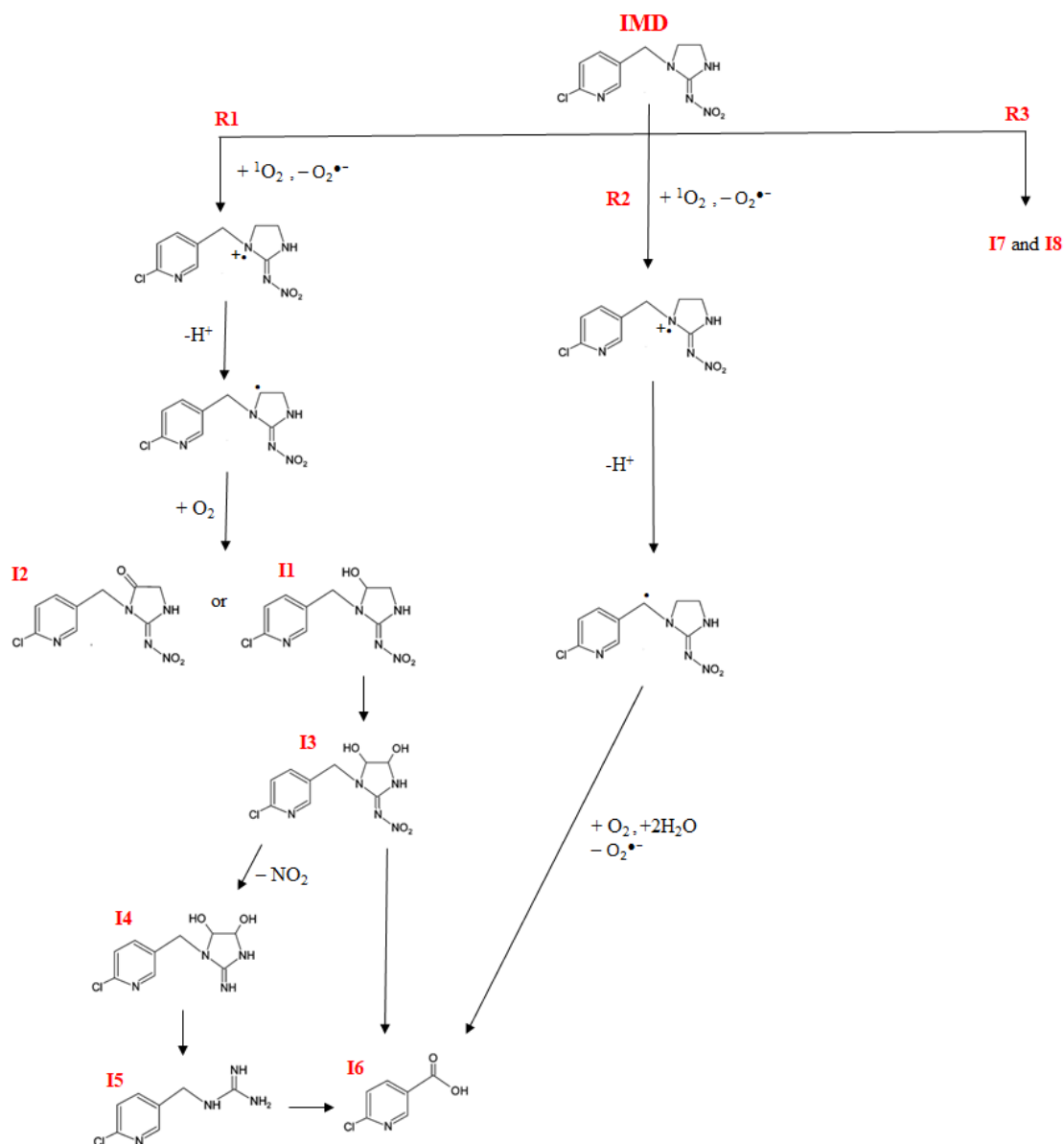


Figure 2.13. IMD degradation pathway in the $\text{Co}_3\text{O}_4/\text{PMS}/\text{SI}$ process.

2.4. Conclusions

Cubic-phase Co_3O_4 nanoparticles were successfully synthesized by a simple precipitation/calcination method. These nanoparticles were then immobilized on glass microfiber substrates, by vacuum filtration deposition from stable suspensions of positively charged aggregates. The photochemical performance of the as-prepared Co_3O_4 coatings for IMD degradation by PMS was investigated using a continuous flow-cell

reactor, with detailed evaluation of the effects of PMS concentration, flow rate, and type of irradiation. Adsorption, photolysis, photocatalysis, and the presence of only PMS were found to lead to negligible IMD removal. The combination of PMS with solar irradiation or with Co_3O_4 led to IMD removals of ~50% and ~70%, respectively. The highest performance (99% removal) was achieved using the Co_3O_4 /PMS/solar irradiation combination, which could be attributed to the synergistic activation of PMS by the UV component of the solar radiation and the Co_3O_4 catalyst. The optimal operational conditions were found to be a PMS concentration of 0.2 g L^{-1} , a flow rate of 0.1 mL min^{-1} (residence time = 77 min), and full-spectrum (solar) irradiation. Under the experimental conditions used in this work, the photogenerated electrons in the Co_3O_4 did not play a significant role, but the electrostatic interaction of PMS and Co_3O_4 considerably increased the efficiency of solar irradiation for the activation of PMS. Sulfate and superoxide radicals, as well as singlet oxygen, were the main active species associated with IMD removal. Eight intermediate degradation products were identified. Finally, it could be concluded that the Co_3O_4 /PMS/solar irradiation technique is capable of providing efficient degradation of IMD in continuous systems, enabling reduction of the PMS concentration and making the process more sustainable.

CHAPTER 3

PEROXYMONOSULFATE ACTIVATION BY MAGNETIC g-C₃N₄/NiFe₂O₄ FOR TETRACYCLINE HYDROCHLORIDE DEGRADATION UNDER VISIBLE LIGHT

3.1. Introduction

Tetracyclines (TCs) are one of the major groups of antibiotics consumed globally, with their high antibacterial activity resulting in widespread applications in the treatment of diseases and for promoting livestock growth. However, they are not fully metabolized by human/animal organisms and cannot be efficiently removed in municipal wastewater treatment plants using conventional techniques, so they are now commonly found in surface water, groundwater, and wastewater. The presence of TCs in water bodies is a potential risk to humans, since it may induce antibiotic resistance in bacteria, leading to the generation of superbacteria [5]. Therefore, it is imperative to develop effective methods for the removal of TCs from wastewaters.

Over the last few years, advanced oxidation processes based on peroxymonosulfate (PMS-AOP) have been intensively investigated for the degradation of several antibiotics, including TCs [94–96]. In these AOPs, PMS can be activated to generate sulfate ($\text{SO}_4^{\bullet-}$), hydroxyl (HO^{\bullet}), and superoxide ($\text{O}_2^{\bullet-}$) radicals, as well as singlet oxygen ($^1\text{O}_2$), which are highly reactive species that are strongly oxidizing towards many organic compounds [20,97,98]. In addition, PMS is inexpensive, easy to transport and store, readily activated over a wide pH range (3-10), and has an asymmetric structure that can facilitate its activation compared to hydrogen peroxide [99]. The activation of PMS is usually achieved using energy (heat, UV light, or ultrasound) or transition metals (in homogenous and heterogeneous processes) [13]. Nevertheless, these traditional PMS-AOP suffer from disadvantages such as high energy consumption and limited peroxymonosulfate activation efficiency [16]. Fortunately, the use of photocatalytic technology to activate PMS can overcome these shortcomings.

Recently, the use of graphitic carbon nitride (g-C₃N₄, CN) as a photocatalyst has attracted particular attention, due to its outstanding properties including high stability, competitive cost, easy fabrication, and narrow band gap (~2.7 eV), with many studies having focused on evaluation of its performance in activating PMS to degrade organic

pollutants under visible light. However, the efficiency of PMS activation by pristine g-C₃N₄ remains far from satisfactory, due to the fast recombination of photogenerated electron-hole pairs and low ability to utilize visible light [20]. To overcome these limitations, several approaches have been proposed, including the coupling of g-C₃N₄ with other semiconductors (such as ZnO [100], Nb₂O₅ [101], Co₃O₄ [102], MoO₃ [103], and Fe₂O₃ [104] to form heterojunctions.

Nickel ferrite (NiFe₂O₄, NFO), in particular, not only has a suitable band position that matches well with that of g-C₃N₄ to form a heterojunction and promote an effective separation of photogenerated charges, but also possesses a narrow band gap of 1.59–2.19 eV and excellent magnetic properties, which can extend the response of the photocatalyst to visible light and facilitate its recovery for the purpose of reuse [22,105]. In addition, as a transition metal oxide, NiFe₂O₄ can activate PMS for the degradation of recalcitrant compounds [106]. There have been some reports concerning the use of g-C₃N₄/NiFe₂O₄ for water treatment. For example, Li et al. [107] synthesized a g-C₃N₄/NiFe₂O₄ heterojunction photocatalyst that showed better performance than g-C₃N₄ alone for degradation of methylene orange dye. Sun et al. [108] prepared a g-C₃N₄/NiFe₂O₄ composite with enhanced activity in the photocatalytic disinfection of *Aspergillus flavus*. Ji et al. [109], Palanivel et al. [22], and Liu et al. [107] prepared NiFe₂O₄/g-C₃N₄ heterostructures and investigated their performance in the degradation of dyes and antibiotics under visible light, in the presence of H₂O₂. However, although previous studies have achieved some advances, there are still no reports concerning the photocatalytic activation of PMS by g-C₃N₄/NiFe₂O₄ for the degradation of organic pollutants.

Therefore, in this work, a g-C₃N₄/NiFe₂O₄ heterojunction (CN/NFO) was prepared and its catalytic activity was tested for activation of PMS used in the degradation of tetracycline hydrochloride (TCH) under visible light (VL) irradiation. The overall performance of the CN/NFO/PMS/VL system was evaluated under different pH conditions and in the presence of typical anions (Cl⁻, SO₄²⁻, NO₃⁻, and HCO₃⁻) found in wastewater. Additionally, the catalyst reusability was investigated in consecutive photocatalytic tests. Finally, quenching experiments were performed to determine the active species generated when CN/NFO/PMS was irradiated with visible light. A possible reaction mechanism for TCH degradation was proposed.

3.2. Experimental

3.2.1. Reagents

Melamine ($C_3H_6N_6$), peroxymonosulfate (PMS, $KHSO_5 \cdot 0.5KHSO_4 \cdot 0.5K_2SO_4$), methanol (MeOH, CH_3OH), p-benzoquinone (p-BQ, $C_6H_4O_2$), furfuryl alcohol (FFA, $C_5H_6O_2$), and tetracycline hydrochloride (TCH, $C_{22}H_{24}N_2O_8 \cdot HCl$) were purchased from Sigma-Aldrich. Ferric nitrate nonahydrate ($Fe(NO_3)_3 \cdot 9H_2O$), citric acid ($C_6H_8O_7$), sodium chloride (NaCl), sodium sulfate (Na_2SO_4), and sodium nitrate ($NaNO_3$) were purchased from Synth. Nickel nitrate hexahydrate ($Ni(NO_3)_2 \cdot 6H_2O$), ethanol (EtOH, C_2H_6O), and tert-butyl alcohol (TBA, $C_4H_{10}O$) were supplied by Neon. Sodium bicarbonate ($NaHCO_3$) was obtained from Qhemis. All chemicals were used as received.

3.2.2. Synthesis and characterization of the g- C_3N_4 , $NiFe_2O_4$, and g- C_3N_4 / $NiFe_2O_4$ photocatalysts

Preparation of g- C_3N_4 was performed by a direct thermal polymerization method [22]. Typically, 5 g of melamine were placed in a closed crucible and calcined in a muffle furnace at 550 °C for 5 h, with heating at a rate of 10 °C min⁻¹. The resulting yellowish product was ground into powder, washed with water, and dried in an oven at 80 °C for 2 h.

$NiFe_2O_4$ was synthesized by a citric acid sol-gel method [22]. In this procedure, 2 mmol of $Fe(NO_3)_3 \cdot 9H_2O$ and 1 mmol of $Ni(NO_3)_2 \cdot 6H_2O$ were dissolved in 5 mL of ethanol, with stirring for 1 h. Addition was then made of 3 mmol of citric acid, with further stirring for 1 h until the solution became viscous. The resulting gel solution was dried in an oven at 120 °C for 2 h. The fluffy brick-red product was ground into powder and calcined at 550 °C for 5 h, using a heating rate of 10 °C min⁻¹, resulting in the formation of a dark grey powder.

For preparation of the g- C_3N_4 / $NiFe_2O_4$ composite, the same procedure was followed. However, after gel formation, 5 g of melamine were added and the mixture was stirred for another 30 min. The product obtained was dried at 120 °C for 2 h, ground into powder, placed in a covered crucible, and heated at 10 °C min⁻¹ to 550 °C, maintained for 5 h [22]. Finally, the resulting brownish powder was washed several times with water and dried in an oven at 80 °C for 2 h.

The materials were characterized by X-ray diffraction (XRD), using a Rigaku Miniflex 600 diffractometer with Cu K α radiation (40 kV, 15 mA, $\lambda = 1.5418 \text{ \AA}$). Transmission electron microscopy (TEM) and high-resolution TEM (HRTEM) images were obtained using an FEI Tecnai G2-F20 microscope. Absorption spectra of the as-prepared samples were acquired using a Shimadzu UV-2600 spectrophotometer, with estimation of the band gap values according to the Tauc plot method [70]. Photoluminescence (PL) analysis was performed using a 355 nm laser (Cobolt Zouk), with the dispersed signal detected using a diffractive spectrometer ($f = 19.3 \text{ cm}$) and a silicon CCD detector (Andor/Idus). X-ray photoelectron spectroscopy (XPS) analyses employed a Scienta Omicron ESCA+ spectrometer coupled to an EA125 hemispherical analyzer, with Al K α excitation ($h\nu = 1486.6 \text{ eV}$). The C 1s, N 1s, Ni 2p, Fe 2p, and O 1s spectra were corrected considering the C 1s peak for adventitious carbon at 284.8 eV. Data analysis employed CasaXPS software. Magnetic measurements were performed using a vibrating sample magnetometer (Model 4500, EG&G Princeton Applied Research), applying an electromagnetic field varying from -10 to 10 kOe.

3.2.3. Photocatalytic experiments

Assessment of the photocatalytic performance of the as-prepared samples was based on the degradation of TCH under visible light irradiation. An aqueous suspension (40 mL) containing 10 mg L⁻¹ TCH and 10 mg of the catalyst was stirred continuously in an orbital shaker, at room temperature. In order to evaluate possible adsorption effects, the suspension was maintained under dark conditions for 30 min, before starting the oxidation by irradiation from a visible light source comprising four fluorescent lamps (Philips TDL, 15 W) and simultaneously adding 0.2 mM of PMS. The experiments were performed for 40 min. Every 10 min, an aliquot of the solution was withdrawn, filtered using a 0.22 μm pore size PVDF membrane, and immediately analyzed using a UV-Vis spectrophotometer (Ultrospec 200 pro) in absorbance mode at 357 nm.

The pH of the TCH solution was adjusted using H₂SO₄ or NaOH (0.1 M), in order to investigate the influence of pH on the degradation rate. The influence of the presence of different anions (at 10 mM) on the degradation was assessed by adding NaNO₃, Na₂SO₄, NaCl, NaHCO₃, and Na₂SO₄. Quenching assays were performed with the addition of CH₃OH (1.0 M), C₄H₁₀O (1.0 M), C₅H₆O₂ (5.0 mM), and C₆H₄O₂ (5.0 mM).

3.3. Results and discussion

3.3.1. g-C₃N₄/NiFe₂O₄ characterizations

The XRD patterns of the as-prepared g-C₃N₄, NiFe₂O₄, and g-C₃N₄/NiFe₂O₄ are shown in Figure 3.1. The pristine g-C₃N₄ exhibited two typical diffraction peaks, at 13.04° and 27.38°, assigned to the (100) and (002) planes, respectively, of the hexagonal g-C₃N₄ phase (JCPDS, 87-1526) [110]. The XRD pattern of the pure NiFe₂O₄ showed a series of diffraction peaks at 18.46°, 30.37°, 35.75°, 37.37°, 43.45°, 53.88°, 57.45°, 63.10°, and 74.65°, corresponding to the (111), (220), (311), (222), (400), (422), (511), (440), and (533) planes, respectively, of cubic NiFe₂O₄ (JCPDS, 89-4927) [22]. All the main characteristic peaks of g-C₃N₄ and NiFe₂O₄ were detected in the XRD pattern of the CN/NFO sample, indicating that NiFe₂O₄ was successfully combined with g-C₃N₄.

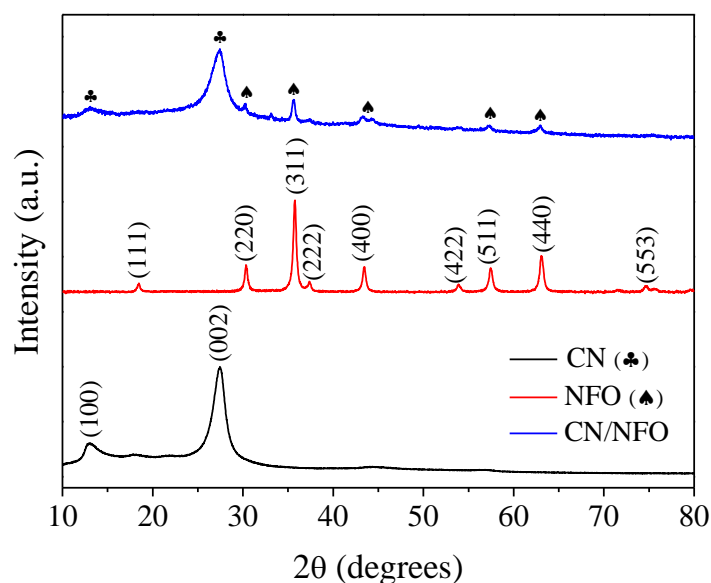


Figure 3.1. XRD patterns of g-C₃N₄, NiFe₂O₄, and g-C₃N₄/ NiFe₂O₄.

This was also confirmed by the TEM images shown in Figures 3.2(a-c), where agglomerates of NiFe₂O₄ particles were observed to be deposited on the surfaces of the g-C₃N₄ sheets [22,112]. Figures 3.2(d-e) show HRTEM images of the g-C₃N₄/NiFe₂O₄ composite, revealing the typical amorphous lamellar structure of g-C₃N₄ and the clear crystal lattice fringes of NiFe₂O₄. The lattice fringes, with d-spacing of 0.25 nm, corresponded to the (311) plane of NiFe₂O₄ [108,113], with the good interfacial contact

with g-C₃N₄ indicating the successful formation of a heterojunction between the two semiconductors.

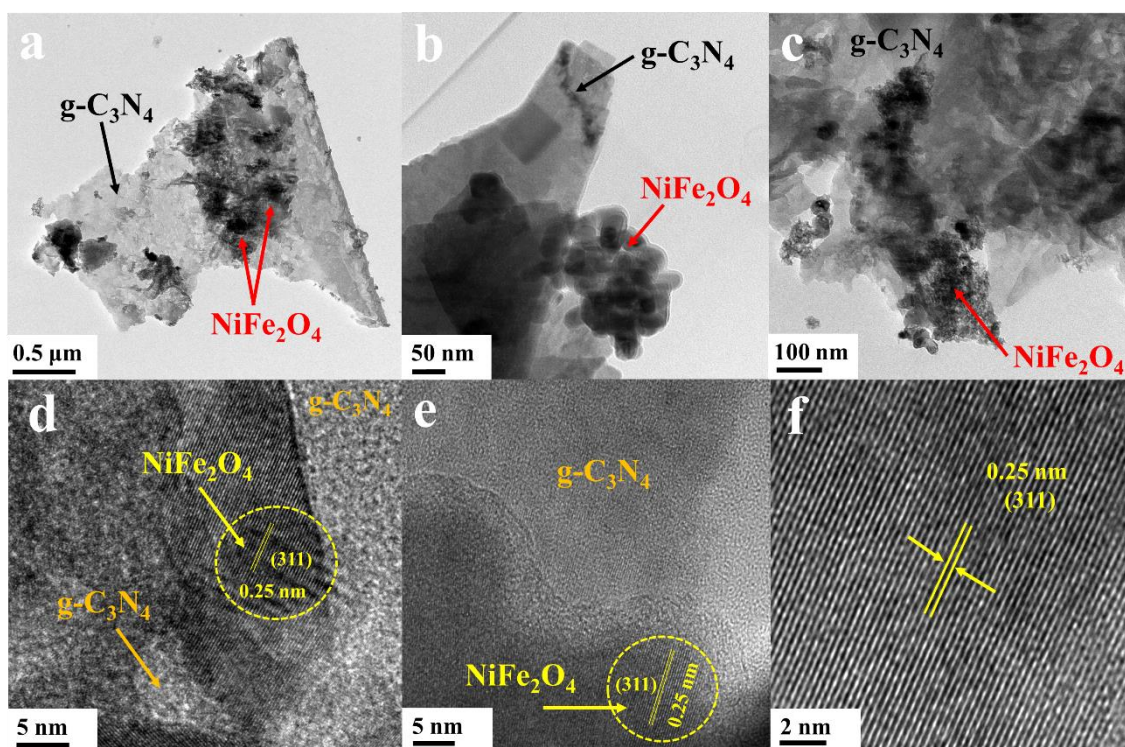


Figure 3.2. TEM (a-c) and HRTEM images (d-f) of g-C₃N₄/NiFe₂O₄.

The XPS measurements (Figure 3.3) confirmed the elemental composition of g-C₃N₄/NiFe₂O₄ and revealed the valence states of the iron and nickel species in the composite. The survey spectrum of the CN/NFO sample (Figure 3.3(a)) confirmed the presence of C, N, O, Fe, and Ni. The high-resolution C 1s, N 1s, O 1s, Fe 2p, and Ni 2p spectra are shown in Figures 3.3(b-f), respectively. The deconvolution of the C 1s spectrum revealed two peaks centered at 284.8 and 287.9 eV (Figure 3.3(b)). The first peak was ascribed to the sp² C-C bonds of the carbon standard employed to calibrate the binding energies, while the second peak was attributed to the sp²-hybridized carbon in N-C=N groups of triazine rings in g-C₃N₄ [114]. The deconvolution of the N 1s spectrum (Figure 3.3(c)) indicated four peaks located at 398.2, 399.2, 400.5, and 404.3 eV. The first three peaks corresponded to the sp² hybridized nitrogen in C-N=C groups of triazine units, tertiary nitrogen (N-(C)₃) groups, and free amino groups (C-N-) in g-C₃N₄, respectively [115]. The weak peak at 404.3 eV could be attributed to charging effects. The deconvolution of the O 1s spectrum (Figure 3.3(d)) identified three peaks at 530.2, 531.8, and 533.4 eV, ascribed to the lattice oxygen in NiFe₂O₄, surface hydroxyl, and

adsorbed water, respectively [115,116]. Deconvolution of the Fe 2p spectrum (Figure 3.3(e)) revealed four peaks at 710.9, 713.8, 718.6, and 724.67 eV, corresponding to Fe 2p_{3/2}, Fe 2p_{3/2}, a satellite peak, and Fe 2p_{1/2}, respectively, indicating that iron was present as Fe³⁺ in the NiFe₂O₄ particles [22,108]. In the Ni 2p spectrum (Figure 3.3(f)), the four deconvoluted peaks were attributed to the Ni 2p_{3/2} (855.8 eV) and Ni 2p_{1/2} (873.5 eV) levels, accompanied by their respective shake-up satellite peaks (861.4 and 879.8 eV), revealing that the nickel in NiFe₂O₄ was in the form of Ni²⁺ [106,108].

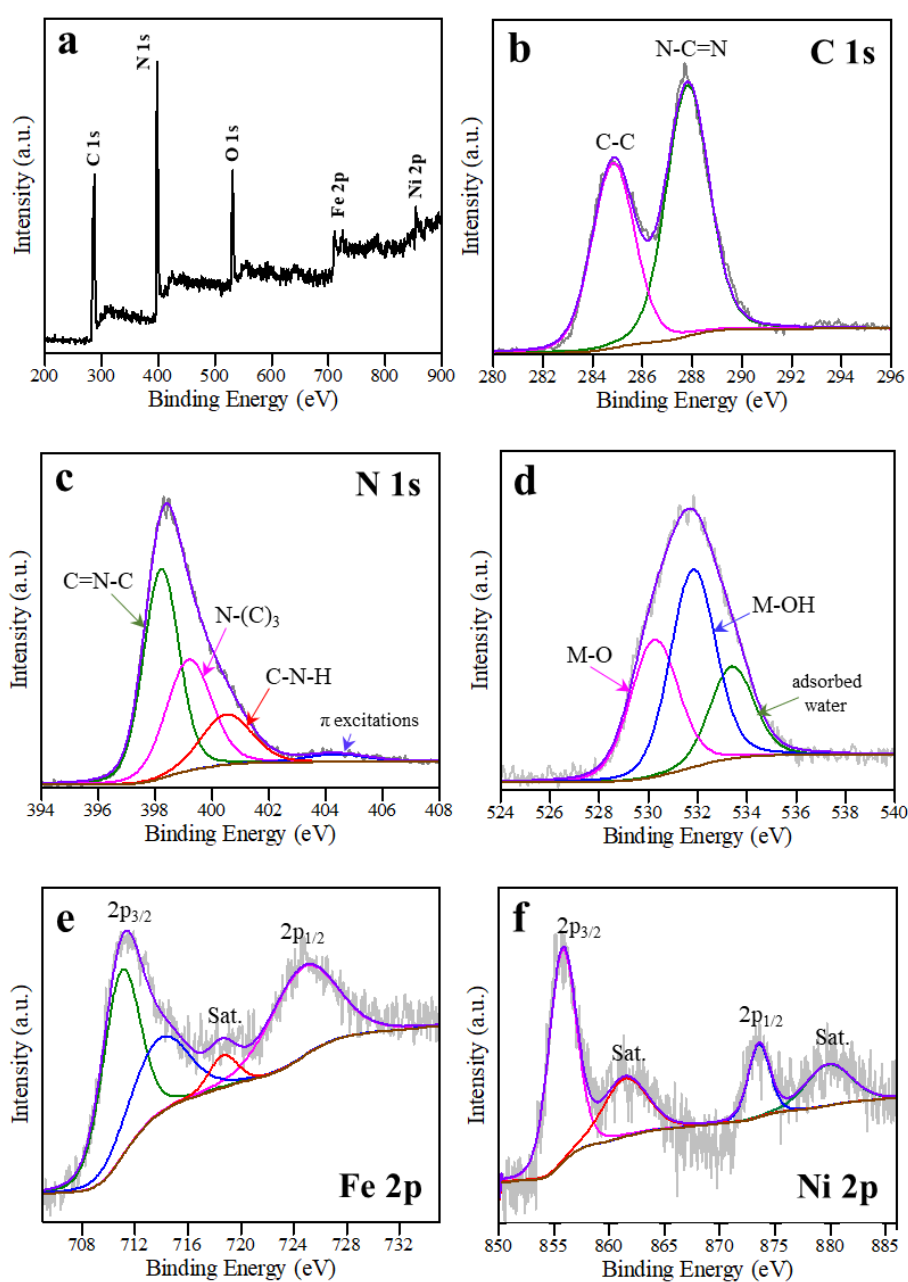


Figure 3.3. XPS survey spectrum (a), and C 1s (b), N 1s (c), O 1s (d), Fe 2p (e), and Ni 2p (f) high resolution spectra of g-C₃N₄/NiFe₂O₄.

The ability of the photocatalysts to absorb light and promote charge carrier separation was investigated by UV-visible diffuse reflectance spectroscopy (DRS) and photoluminescence (PL), respectively. Figure 3.4(a) shows the UV-Vis absorption spectra for g-C₃N₄, NiFe₂O₄, and the g-C₃N₄/NiFe₂O₄ composite. Compared to the pure g-C₃N₄, the spectrum for the CN/NFO composite showed a red shift of the absorption edge towards the visible light region, which is highly desirable for photocatalytic purposes. The direct band gap energies (E_g) of the materials (Figure 3.4(b)) were estimated using the Tauc method [70], with values of approximately 2.72 and 1.68 eV obtained for g-C₃N₄ and NiFe₂O₄, respectively, in good agreement with previous results [22,108].

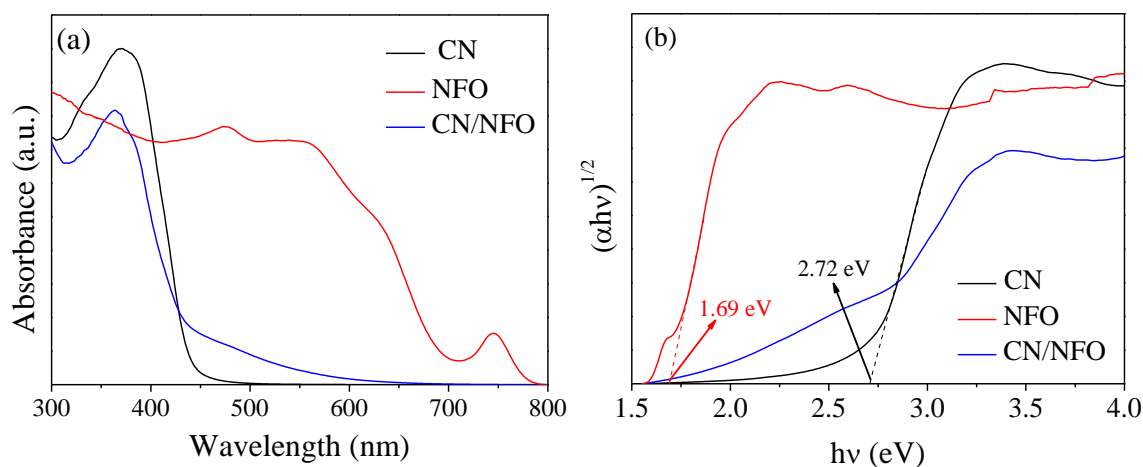


Figure 3.4. UV-Vis absorption spectra (a) and Tauc plots (b) of the photocatalysts.

Figure 3.5 displays the PL spectra of the g-C₃N₄ and g-C₃N₄/NiFe₂O₄ photocatalysts. For g-C₃N₄, a strong and broad emission peak was observed at ~472 nm, while the intensity of this peak was significantly reduced after combination with NiFe₂O₄, indicating a lower recombination rate of the photogenerated charge carriers in the composite [22,115,117]. These results were suggestive of intimate interfacial contact between g-C₃N₄ and NiFe₂O₄, consistent with the HRTEM images, which facilitated separation of the photogenerated electron-hole pairs and suppressed their recombination.

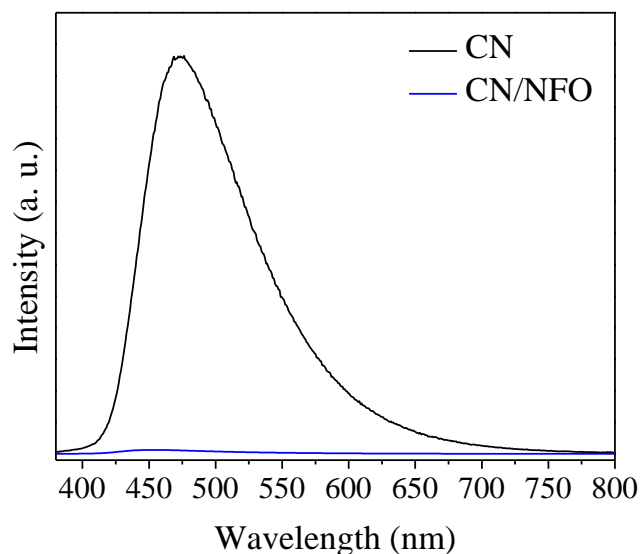


Figure 3.5. PL spectra of the photocatalysts.

The magnetic properties of $g\text{-C}_3\text{N}_4/\text{NiFe}_2\text{O}_4$ were analyzed using a vibrating sample magnetometer (VSM). Figures 3.6(a-b) show the magnetization curves for NiFe_2O_4 and $g\text{-C}_3\text{N}_4/\text{NiFe}_2\text{O}_4$, with saturation magnetizations of 34.13 and 2.00 emu g^{-1} , respectively. Although the magnetic property of CN/NFO was much lower than that of pure ferrite, due to the presence of non-magnetic $g\text{-C}_3\text{N}_4$ in the composite [22], it was sufficient to allow separation of the particles from the solution by the application of an external magnetic field, consequently increasing the recyclability of the material and its potential for use in industrial applications.

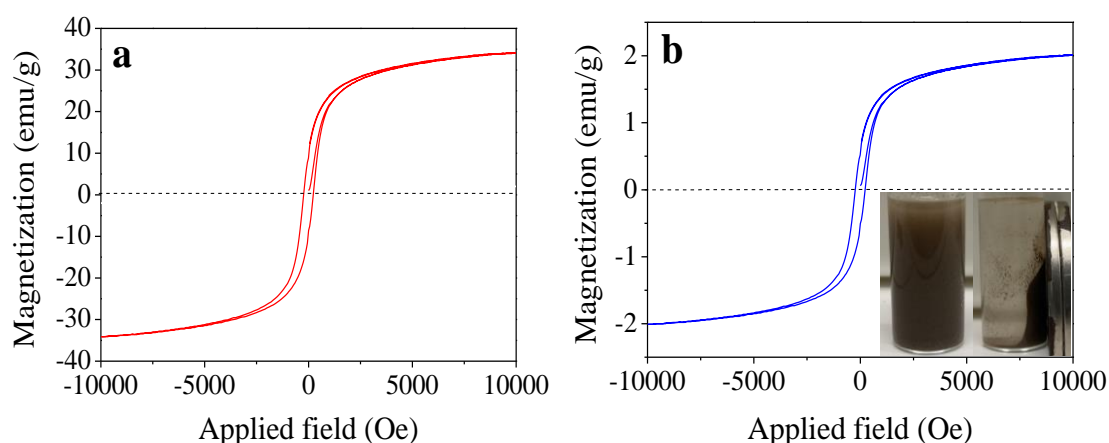


Figure 3.6. Magnetization hysteresis loops of NiFe_2O_4 (a) and $g\text{-C}_3\text{N}_4/\text{NiFe}_2\text{O}_4$ (b).

3.3.2. Photocatalytic activity evaluation

The photocatalytic performances of the fabricated materials for activating PMS were evaluated using the degradation of tetracycline hydrochloride under visible light irradiation. Figure 3.7 shows the TCH degradation kinetics for different reaction conditions, expressed in terms of the normalized TCH concentration (C/C_0). For the CN/NFO/VL photocatalytic and PMS/VL photooxidation systems the degradation efficiencies were only 24% and 45%, respectively, while photolysis was negligible during the 40 min reaction. Evaluation was also made of PMS activated by $g\text{-C}_3\text{N}_4$ or NiFe_2O_4 alone, under visible light irradiation, resulting in approximately 69% and 65% removals using the CN/PMS/VL and NFO/PMS/VL systems, respectively. Finally, the combination of $g\text{-C}_3\text{N}_4/\text{NiFe}_2\text{O}_4$, PMS, and visible light irradiation resulted in a substantial acceleration of TCH degradation, achieving 86% removal, indicating a synergism between the CN/NFO heterojunction photocatalyst and PMS activation. This synergistic effect became more evident at 10 min, when the degradation efficiency exhibited by the composite was approximately 23% higher than obtained for the sum of the individual systems (CN/PMS/VL + NFO/PMS/VL). The better performance of the CN/NFO heterojunction could be attributed to its greater light absorption capacity and fast separation of the photogenerated charges during the photocatalytic process.

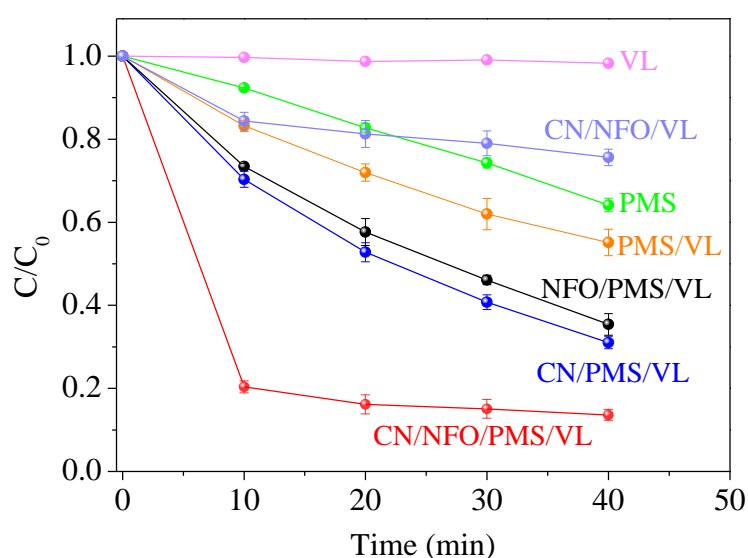


Figure 3.7. Normalized TCH degradation over time, under different reaction conditions: —●— photolysis; —●— PMS only; —■— photocatalysis (in the absence of PMS); —■— PMS and VL; —●— NiFe_2O_4 and PMS under VL; —●— $g\text{-C}_3\text{N}_4$ and PMS under VL; —●— $g\text{-C}_3\text{N}_4/\text{NiFe}_2\text{O}_4$ and PMS under VL.

Figure 3.8 shows the results for assessment of CN/NFO stability by using the same photocatalyst in three degradation cycles. The photodegradation efficiency remained above 80%, indicating the good stability of the synthesized photocatalyst. In addition, evaluation was made of the photocatalytic performance of the CN/NFO composite at different initial pH values (3, 6, 7, 8, and 9) and in the presence of various anions typically found in real wastewater (NO_3^- , SO_4^{2-} , Cl^- , and HCO_3^-), as shown in Figures 3.9 and 3.10, respectively. The natural pH of the TCH solution was 4.6. Alteration of the initial pH from 3 to 9 had no significant effect on TCH degradation efficiency indicating that the CN/NFO/PMS/VL system could operate effectively over a wide pH range, making it highly advantageous, when compared to the traditional Fenton process performed in a narrow pH range.

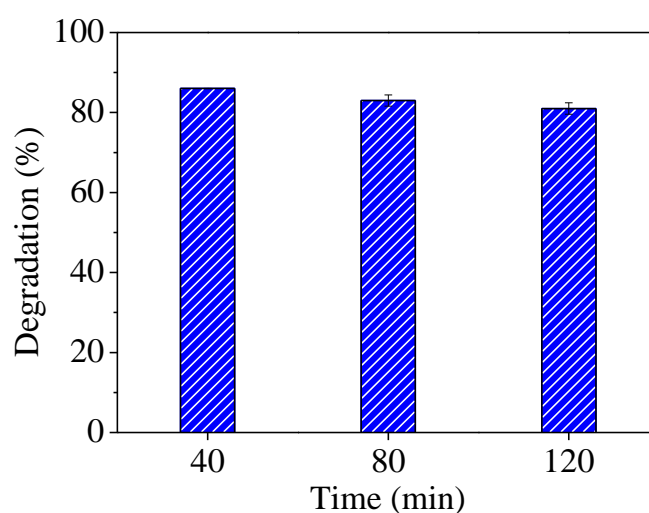


Figure 3.8. Reuse tests using CN/NFO.

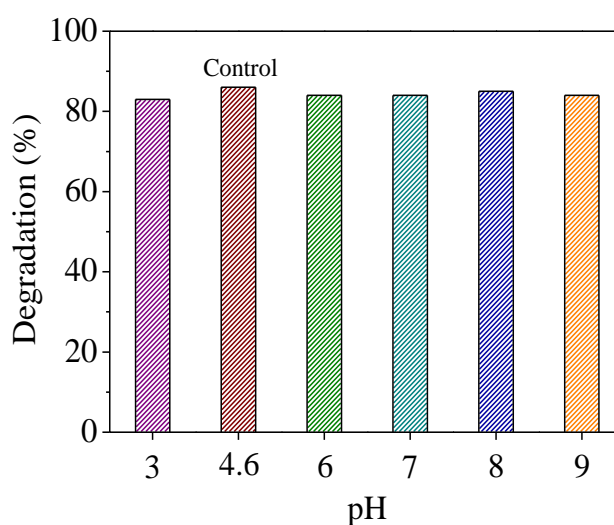


Figure 3.9. Effect of initial pH on TCH degradation performance. Note: Control refers to the TCH solution without pH adjustment.

Regarding the effect of the co-existence of other anions on TCH removal, it is known that the presence of nitrate, sulfate, chloride, and bicarbonate in wastewater can affect the removal of pollutants in AOP, since the adsorption of the anions can block the active sites of the catalyst and/or they may react rapidly with the free radicals, capturing them and consequently decreasing the photocatalytic degradation efficiency [16,106]. As shown in Figure 3.10, the effects of NO_3^- , SO_4^{2-} , and Cl^- on TCH removal were not significant, while HCO_3^- had a moderate impact on the performance of the CN/NFO/PMS/VL system. This could be explained by the fact that HCO_3^- can capture some oxidizing species, such as $\text{SO}_4^{\bullet-}$ and HO^{\bullet} radicals [34,66]. Nevertheless, in the presence of these anions, the CN/NFO/PMS/VL system still presented satisfactory performance during 40 min of reaction.

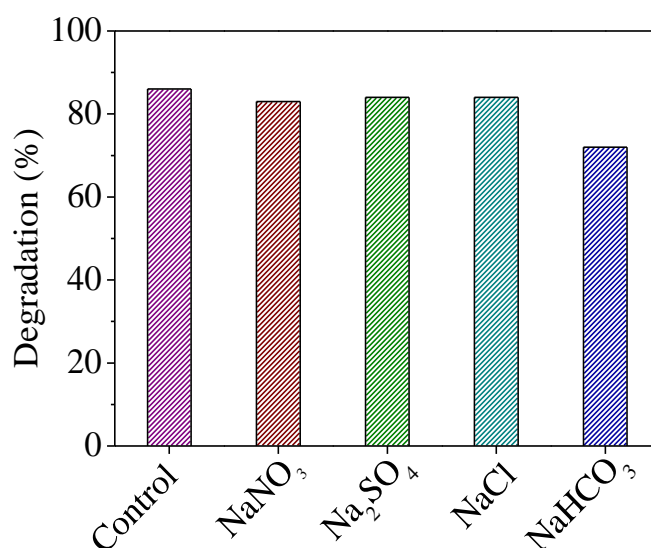


Figure 3.10. Effects of NO_3^- , SO_4^{2-} , Cl^- , and HCO_3^- on TCH degradation performance.

Note: Control refers to the TCH solution without addition of anions.

Table 3.1 summarizes the degradation performance obtained in this work, comparing it with similar studies reported in the literature. It should be highlighted that CN/NFO presented similar performance to other photocatalysts, but with a substantially lower PMS dosage.

Table 3.1. TC degradation efficiencies achieved using different photocatalytic/PMS systems under visible light irradiation.

Catalyst	[TC] (mg L ⁻¹)	Catalyst (g L ⁻¹)	[PMS] (mM)	Time (min)	Removal (%)	Ref.
BC/CN-15	10	0.20	0.65	60	88.3	[118]
CuBi ₂ O ₄ /BiOBr	10	0.20	2.0	35	90.30	[119]
MCN/NCDs	10	0.50	0.5	60	98.4	[120]
CuBi ₂ O ₄ /MnO ₂	5	0.30	1.3	40	97.6	[78]
FCN-12	30	0.60	1.3	120	83.4	[121]
NiFe ₂ O ₄ /g-C ₃ N ₄	10	0.25	0.2	10	80.0	This work

3.3.3. Mechanism of TCH degradation by the CN/NFO/PMS/VL system

Quenching experiments were performed to identify the main active species and propose a reaction mechanism for TCH degradation using the CN/NFO/PMS/VL system. Based on a previous literature search for the active species generated by photocatalysis and PMS activation, it was speculated that SO₄^{•-}, HO[•], O₂^{•-}, and ¹O₂ might be involved in the degradation of TCH by the CN/NFO/PMS/VL system [22,43,106]. Therefore, in order to verify this hypothesis, p-BQ and FFA were used to trap O₂^{•-} and ¹O₂, respectively, while TBA and MeOH were used to identify the roles of SO₄^{•-} and HO[•] on TCH degradation. MeOH can react efficiently with both HO[•] ($k = 9.7 \times 10^8 \text{ M}^{-1} \text{ s}^{-1}$) and SO₄^{•-} ($k = 2.5 \times 10^7 \text{ M}^{-1} \text{ s}^{-1}$), while TBA is a selective scavenger for HO[•] ($k = 3.8\text{-}7.6 \times 10^8 \text{ M}^{-1} \text{ s}^{-1}$) rather than SO₄^{•-} ($k = 4.0\text{-}9.5 \times 10^5 \text{ M}^{-1} \text{ s}^{-1}$) [122,123]. As shown in Figure 3.11, the TCH degradation efficiency decreased from 86% to 62, 60, 25, and 14% after the addition of MeOH, TBA, p-BQ, and FFA, respectively. These results indicated that O₂^{•-} and ¹O₂ were the dominant active species in the NFO/CN/PMS/VL system, while HO[•] played a secondary role. Curiously, the results showed that SO₄^{•-} had a negligible effect on TCH removal. The fact that only HO[•] was detected, while no SO₄^{•-} effect was observed, suggested that SO₄^{•-} was unstable during the CN/NFO/PMS/VL process and was rapidly replaced by HO[•] via oxidation of H₂O (Equation 3.14). Similar observations have been reported in previous studies [124,125].

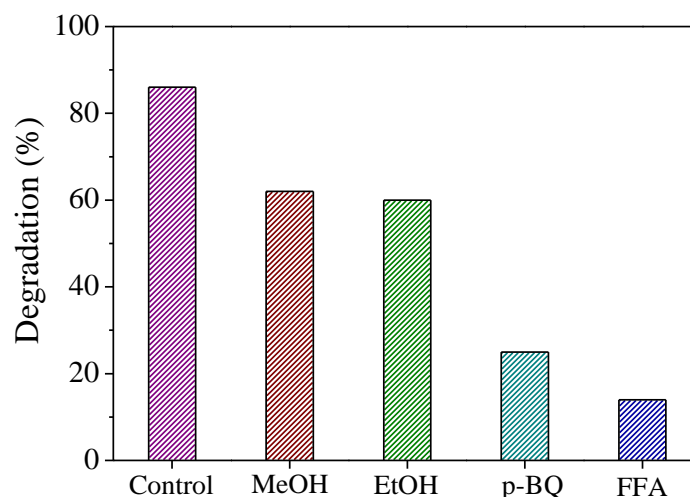


Figure 3.11. Effects of different quenchers on TCH degradation using the CN/NFO/PMS/VL system. Note: Control refers to the TCH solution without quenchers.

Based on the above results, a possible mechanism was proposed for TCH degradation using the CN/NFO/PMS/VL system (Equations 3.1-3.16, Figure 3.12). In previous studies, the valence band (VB) and conduction band (CB) edges of pure g-C₃N₄ and NiFe₂O₄ were determined to be 1.55/-1.13 V and 1.92/0.24 V, respectively, and a type-II heterojunction could be formed. Hence, upon visible light irradiation, both g-C₃N₄ and NiFe₂O₄ could absorb photons and generate electrons and holes (Equation 3.1). Subsequently, the electrons from the g-C₃N₄ conduction band were transferred to the CB of NiFe₂O₄, while the holes from the VB of NiFe₂O₄ were transferred to the VB of g-C₃N₄, consequently reducing the recombination rate of the photogenerated carriers [22,111]. On the one hand, the valence and conduction band positions of g-C₃N₄ (1.55 V) and NiFe₂O₄ (0.24 V) do not have sufficient energy to drive the typical photocatalytic reactions (H₂O/HO[•], 2.72 V; O₂/O₂^{•-}, -0.33 V). On the other hand, the CB potential of g-C₃N₄ is more negative than that of O₂/O₂^{•-} (Equation 3.2) [97]. Therefore, a portion of the electrons of the g-C₃N₄ conduction band were captured by the adsorbed oxygen to generate O₂^{•-} (Equation 3.2) [22,111], while the electrons accumulated in the NiFe₂O₄ conduction band were captured by PMS to produce SO₄^{•-} and HO[•] (Equations 3.3-3.4) [115]. Besides, the position of the CB of NiFe₂O₄ is lower than the standard potential of Fe³⁺/Fe²⁺ (0.77 V); thus, Fe³⁺ species in NiFe₂O₄ could be reduced to Fe²⁺ (Equation 3.5) [107]. Meanwhile, the Ni²⁺ and Fe²⁺ ions on the catalyst surface could react with PMS for the generation of SO₄^{•-} (Equations 3.6-3.7), being oxidized to Ni³⁺ and Fe³⁺, which in turn could also activate PMS, but generating the less oxidizing species SO₅^{•-} (Equations

3.8-3.9). In parallel, the photogenerated electrons assisted in regenerating Ni^{2+} and Fe^{2+} (Equations 3.5 and 3.10), accelerating the reaction between Ni/Fe and PMS, while further inhibiting the recombination of e^-/h^+ pairs [43,106,115]. Furthermore, $\text{SO}_4^{\bullet-}$ and HO^\bullet radicals could also be obtained by the interaction of light with PMS (Equation 3.11) [115,119]. Next, the $\text{O}_2^{\bullet-}$, $\text{SO}_4^{\bullet-}$, and $\text{SO}_5^{\bullet-}$ radicals generated during the process were converted to $^1\text{O}_2$ and HO^\bullet , according to Equations 3.12-3.15 [43,66,121]. Finally, $\text{O}_2^{\bullet-}$, $^1\text{O}_2$, and HO^\bullet oxidized the TCH (Equation 3.16), providing a remarkable degradation performance.



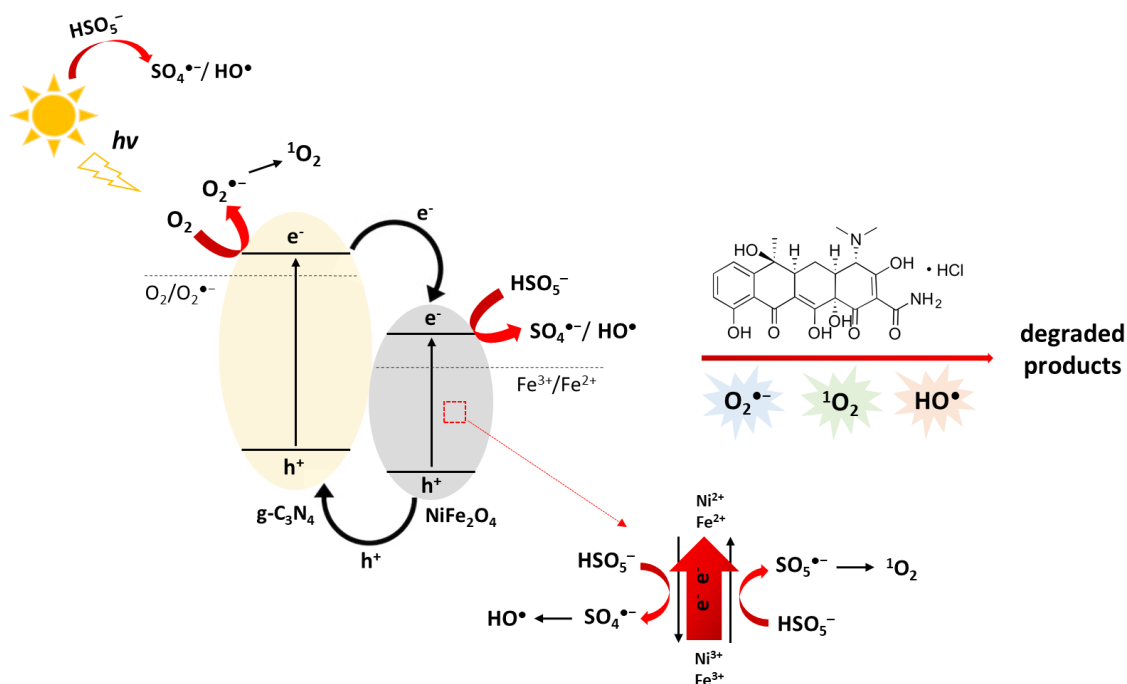


Figure 3.12. Proposed mechanism for TCH degradation by CN/NFO composite in presence of PMS and visible light.

3.4. Conclusions

In this study, the $\text{NiFe}_2\text{O}_4/\text{g-C}_3\text{N}_4$ composite was synthesized by a facile sol-gel method and was applied to activate PMS for the degradation of TCH under visible light irradiation. In comparison with the $\text{g-C}_3\text{N}_4$ and NiFe_2O_4 systems alone, the CN/NFO/PMS/VL system presented the highest photocatalytic degradation performance, achieving 86% degradation of TCH within 40 min. Furthermore, the photocatalytic performance of the CN/NFO/PMS/VL system remained robust under various conditions (recycling, different initial pH values, and presence of co-existing anions). The excellent degradation efficiency of the CN/NFO/PMS/VL system towards TCH could be attributed to heterojunction formation between CN and NFO, which facilitated the separation and transfer of the photogenerated charge carriers, consequently accelerating the reaction between photogenerated electrons, Ni/Fe species and PMS. Trapping experiments revealed that $\text{O}_2^{\bullet-}$, $^1\text{O}_2$, and HO^\bullet were the main active species involved in the TCH degradation process. In conclusion, this work provides a new path for the degradation of organic pollutants in water.

CHAPTER 4

CONCLUSIONS AND SUGGESTIONS FOR FUTURE WORKS

Cobalt oxide and carbon nitride/nickel ferrite composite demonstrated to be efficient catalysts for the degradation of organic pollutants in the presence of peroxymonosulfate and solar/visible light. Regarding the first one, it was verified that under the experimental conditions used in this work, the photogenerated electrons in Co_3O_4 did not play a significant role in activating PMS. Although PMS can be usually activated by photogenerated electrons in the conduction band of photocatalysts, pristine Co_3O_4 has a narrow band gap, so that the electrons and holes formed upon its excitation under light irradiation are likely prone to recombination, making it difficult for Co_3O_4 to provide electrons for PMS activation. Hence, the main factor identified as responsible for enhancing the performance of the Co_3O_4 /PMS/SI system was the electrostatic interaction between PMS (negatively charged) and Co_3O_4 (positively charged), which could weaken the bonds of PMS and facilitate its activation by the UV component of solar light.

Regarding the second material, the heterojunction formed between g- C_3N_4 and NiFe_2O_4 was effective in increasing the electron lifetime because of the band edges positions of the different semiconductors, creating a gradient in the energy levels and allowing the spatial separation of the photogenerated charges, that is, electrons were transferred to the CB of NiFe_2O_4 , while holes were transferred to VB of g- C_3N_4 . The synergistic effect between the photogenerated electrons, Ni/Fe species on the catalyst structure, and PMS was pointed as the main reason for the remarkable performance of g- C_3N_4 / NiFe_2O_4 in TCH photooxidation. Overall, both approaches developed in this thesis work show great promise for environmental remediation applications in which the degradation of organic pollutants is desired.

Suggestions for Future Works

New insights into the performance and reaction mechanism of Co_3O_4 and g- C_3N_4 / NiFe_2O_4 in PMS-assisted photocatalytic processes have been achieved in this thesis work. However, other studies must be conducted to further improve and optimize the photocatalyst-activated PMS technology, especially for large-scale applications. In this regard, the following suggestions are proposed for future works:

- The importance of constructing a heterojunction to enable the utilization of photogenerated electrons in PMS activation was evidenced in this study. Therefore, it is suggested to couple Co_3O_4 with another semiconductor in order to further enhance its performance towards the degradation of organic compounds.

- The photocatalytic assays conducted on the $\text{g-C}_3\text{N}_4/\text{NiFe}_2\text{O}_4/\text{PMS}/\text{VL}$ system in the presence of co-existing anions revealed that certain ions, such as bicarbonate, can reduce the degradation efficiency since they can trap the oxidizing species responsible for the degradation of organic compounds, especially sulfate and hydroxyl radicals. Therefore, it is essential to assess how the presence of these anions in the reaction medium affects the performance of the $\text{Co}_3\text{O}_4/\text{PMS}/\text{SI}$ system.

- In a literature review, it was identified that among the degradation products detected in the $\text{Co}_3\text{O}_4/\text{PMS}/\text{SI}$ system, one of them may be more toxic to certain aquatic organisms than the initial compound. Therefore, it is suggested for future works to conduct toxicity assessments in order to ensure a better comprehension of the impact of reaction intermediates. Similarly, it is also important to identify the degradation products of the $\text{g-C}_3\text{N}_4/\text{NiFe}_2\text{O}_4/\text{PMS}/\text{VL}$ process and evaluate their toxicity.

REFERENCES

- [1] I. Som, M. Roy, R. Saha, Advances in Nanomaterial-based Water Treatment Approaches for Photocatalytic Degradation of Water Pollutants, *ChemCatChem*. 12 (2020) 3409–3433. doi:10.1002/cctc.201902081.
- [2] F. Lu, D. Astruc, Nanocatalysts and other nanomaterials for water remediation from organic pollutants, *Coord. Chem. Rev.* 408 (2020) 213180. doi:10.1016/j.ccr.2020.213180.
- [3] W.F. Young, H. Horth, R. Crane, T. Ogden, Taste and odour threshold concentrations of potential potable water contaminants, *Water Res.* 30 (1996) 331–340. doi:10.1016/0043-1354(95)00173-5.
- [4] N. John, A. V Koehler, B.R.E. Ansell, L. Baker, N.D. Crosbie, A.R. Jex, An improved method for PCR-based detection and routine monitoring of geosmin-producing cyanobacterial blooms, *Water Res.* 136 (2018) 34–40. doi:10.1016/j.watres.2018.02.041
- [5] J. Scaria, K. V Anupama, P. V Nidheesh, Tetracyclines in the environment : An overview on the occurrence , fate , toxicity , detection , removal methods , and sludge management, *Sci. Total Environ.* 771 (2021) 145291. doi:10.1016/j.scitotenv.2021.145291.
- [6] J.B. Ellis, Pharmaceutical and personal care products (PPCPs) in urban receiving waters, *Environ. Pollut.* 144 (2006) 184–189. doi:10.1016/j.envpol.2005.12.018.
- [7] L. He, J. Zhi, H. Li, Y. Jia, Q. Gao, J. Wang, Y. Xu, X. Li, Peroxymonosulfate activation by magnetic NiCo layered double hydroxides for naproxen degradation, *Colloids Surfaces A Physicochem. Eng. Asp.* 642 (2022) 128696. doi:10.1016/j.colsurfa.2022.128696.
- [8] N. Mumtaz, A. Javaid, M. Imran, S. Latif, N. Hussain, S. Nawaz, M. Bilal, Nanoengineered metal-organic framework for adsorptive and photocatalytic mitigation of pharmaceuticals and pesticide, *Environ. Manage.* 308 (2022) 119690. doi:10.1016/j.envpol.2022.119690.
- [9] Two billion people lack safe drinking water, more than twice lack safe sanitation. Available on: <<https://www.unicef.org/philippines/press-releases/two-billion-people-lack-safe-drinking-water-more-twice-lack-safe-sanitation>> (accessed May 1, 2023).
- [10] H. Ritchi, M. Roser. Clean Water. Available on:

<<https://ourworldindata.org/water-access>> (accessed May 1, 2023).

- [11] M.O. Barbosa, N.F.F. Moreira, A.R. Ribeiro, M.F.R. Pereira, Occurrence and removal of organic micropollutants : An overview of the watch list of EU Decision 2015/495, *Water Res.* 94 (2016) 257–259. doi:10.1016/j.watres.2016.02.047.
- [12] L. Yao, X. He, J. Lv, G. Xu, Z. Bao, J. Cui, D. Yu, Y. Wu, Efficient degradation of ciprofloxacin by $\text{Co}_3\text{O}_4/\text{Si}$ nanoarrays heterojunction activated peroxymonosulfate under simulated sunlight: Performance and mechanism, *J. Environ. Chem. Eng.* 10 (2022) 107397. doi:10.1016/j.jece.2022.107397.
- [13] F. Ghanbari, M. Moradi, Application of peroxymonosulfate and its activation methods for degradation of environmental organic pollutants: Review, *Chem. Eng. J.* 310 (2017) 41–62. doi:10.1016/j.cej.2016.10.064.
- [14] L. Kong, G. Fang, X. Xi, Y. Wen, Y. Chen, M. Xie, F. Zhu, A novel peroxymonosulfate activation process by periclyase for efficient singlet oxygen-mediated degradation of organic pollutants, *Chem. Eng. J.* 403 (2021) 126445. doi:10.1016/j.cej.2020.126445.
- [15] A. Hassani, J. Scaria, F. Ghanbari, P. V Nidheesh, Sulfate radicals-based advanced oxidation processes for the degradation of pharmaceuticals and personal care products : A review on relevant activation mechanisms , performance , and perspectives, *Environ. Res.* 217 (2023) 114789. doi:10.1016/j.envres.2022.114789.
- [16] C.H. Shen, X.J. Wen, Z.H. Fei, Z.T. Liu, Q.M. Mu, Visible-light-driven activation of peroxymonosulfate for accelerating ciprofloxacin degradation using $\text{CeO}_2/\text{Co}_3\text{O}_4$ p-n heterojunction photocatalysts, *Chem. Eng. J.* 391 (2020) 123612. doi:10.1016/j.cej.2019.123612.
- [17] S. He, Y. Chen, X. Li, L. Zeng, M. Zhu, Heterogeneous Photocatalytic Activation of Persulfate for the Removal of Organic Contaminants in Water: A Critical Review, *ACS ES&T Eng.* 2 (2022) 527–546. doi:10.1021/acsestengg.1c00330.
- [18] P. Shi, R. Su, S. Zhu, M. Zhu, D. Li, S. Xu, Supported cobalt oxide on graphene oxide : Highly efficient catalysts for the removal of Orange II from water, *J. Hazard. Mater.* 229–230 (2012) 331–339. doi:10.1016/j.jhazmat.2012.06.007.
- [19] Y. Wang, L. Zhou, X. Duan, H. Sun, E.L. Tin, W. Jin, S. Wang, Photochemical degradation of phenol solutions on Co_3O_4 nanorods with sulfate radicals, *Catal. Today.* 258 (2015) 576–584. doi:10.1016/j.cattod.2014.12.020.
- [20] J. Tan, Z. Li, J. Li, Y. Meng, X. Yao, Y. Wang, Y. Lu, T. Zhang, Visible-light-

- assisted peroxymonosulfate activation by metal-free bifunctional oxygen-doped graphitic carbon nitride for enhanced degradation of imidacloprid: Role of non-photochemical and photocatalytic activation pathway, *J. Hazard. Mater.* 423 (2022) 127048. doi:10.1016/j.jhazmat.2021.127048.
- [21] A. Balakrishnan, M. Chinthala, Comprehensive review on advanced reusability of g-C₃N₄ based photocatalysts for the removal of organic pollutants, *Chemosphere*. 297 (2022) 134190. doi:10.1016/j.chemosphere.2022.134190.
- [22] B. Palanivel, C. Ayappan, V. Jayaraman, S. Chidambaram, R. Maheswaran, A. Mani, Inverse spinel NiFe₂O₄ deposited g-C₃N₄ nanosheet for enhanced visible light photocatalytic activity, *Mater. Sci. Semicond. Process.* 100 (2019) 87–97. doi:10.1016/j.mssp.2019.04.040.
- [23] H. Luo, Y. Zeng, D. He, X. Pan, Application of iron-based materials in heterogeneous advanced oxidation processes for wastewater treatment : A review, *Chem. Eng. J.* 407 (2021) 127191. doi:10.1016/j.cej.2020.127191.
- [24] P. Taylor, J.L. Wang, L.E.J.I.N. Xu, Advanced Oxidation Processes for Wastewater Treatment : Formation of Hydroxyl Radical and Application Advanced Oxidation Processes for Wastewater Treatment : Formation of Hydroxyl Radical, *Crit. Rev. Environ. Sci. Technol.* 42 (2011) 37–41. doi:10.1080/10643389.2010.507698.
- [25] C. Amor, L. March, M.S. Lucas, J.A. Peres, Application of Advanced Oxidation Processes for the Treatment of Recalcitrant Agro-Industrial Wastewater : A Review, *Water*. 2 (2019) 1–29. doi:10.3390/w11020205.
- [26] F. Ghanbari, M. Moradi, Application of peroxymonosulfate and its activation methods for degradation of environmental organic pollutants : Review, *Chem. Eng. J.* 310 (2017) 41–62. doi:10.1016/j.cej.2016.10.064.
- [27] Q. Yang, Y. Ma, F. Chen, F. Yao, J. Sun, S. Wang, K. Yi, Recent advances in photo-activated sulfate radical-advanced oxidation process (SR-AOP) for refractory organic pollutants removal in water, *Chem. Eng. J.* 378 (2019) 122149. doi:10.1016/j.cej.2019.122149.
- [28] K. Raghava, C.H. Venkata, M.N. Nadagouda, N.P. Shetti, S. Jaesool, T.M. Aminabhavi, Polymeric graphitic carbon nitride (g-C₃N₄)-based semiconducting nanostructured materials : Synthesis methods , properties and photocatalytic applications, 238 (2019) 25–40. doi:10.1016/j.jenvman.2019.02.075.
- [29] R.R. Solís, F.J. Rivas, A.M. Chávez, D.D. Dionysiou, Peroxymonosulfate/solar

- radiation process for the removal of aqueous microcontaminants . Kinetic modeling , influence of variables and matrix constituents, *J. Hazard. Mater.* 400 (2020) 123118. doi:10.1016/j.jhazmat.2020.123118.
- [30] D.T. Oyekunle, E.A. Gendy, J. Ifthikar, Z. Chen, Heterogeneous activation of persulfate by metal and non-metal catalyst for the degradation of sulfamethoxazole: A review, *Chem. Eng. J.* 437 (2022) 135227. doi:10.1016/j.cej.2022.135277.
- [31] S. Xiao, M. Cheng, H. Zhong, Z. Liu, Y. Liu, X. Yang, Q. Liang, Iron-mediated activation of persulfate and peroxymonosulfate in both homogeneous and heterogeneous ways: A review, *Chem. Eng. J.* 384 (2020) 123265. doi:10.1016/j.cej.2019.123265.
- [32] K. Kabra, R. Chaudhary, R.L. Sawhney, Treatment of Hazardous Organic and Inorganic Compounds through Aqueous-Phase Photocatalysis: A Review, *Ind. Eng. Chem. Res.* 43 (2004) 7683–7696. doi:10.1021/ie0498551.
- [33] G.P. Anipsitakis, E. Stathatos, D.D. Dionysiou, Heterogeneous activation of Oxone using Co_3O_4 , *J. Phys. Chem. B.* 109 (2005) 13052–13055. doi:10.1021/jp052166y.
- [34] J. Hu, X. Zeng, G. Wang, B. Qian, Y. Liu, X. Hu, B. He, L. Zhang, X. Zhang, Modulating mesoporous Co_3O_4 hollow nanospheres with oxygen vacancies for highly efficient peroxymonosulfate activation, *Chem. Eng. J.* 400 (2020) 125869. doi:10.1016/j.cej.2020.125869.
- [35] X. Chen, J. Chen, X. Qiao, D. Wang, X. Cai, Performance of nano- Co_3O_4 /peroxymonosulfate system: Kinetics and mechanism study using Acid Orange 7 as a model compound, *Appl. Catal. B Environ.* 80 (2008) 116–121. doi:10.1016/j.apcatb.2007.11.009.
- [36] Y. Zhiyong, M. Bensimon, D. Laub, L. Kiwi-minsker, W. Jardim, Accelerated photodegradation (minute range) of the commercial azo-dye Orange II mediated by Co_3O_4 /Raschig rings in the presence of oxone, *J. Mol. Catal. A Chem.* 272 (2007) 11–19. doi:10.1016/j.molcata.2007.03.023.
- [37] X. Wang, K. Maeda, A. Thomas, K. Takanabe, G. Xin, J.M. Carlsson, K. Domen, M. Antonietti, A metal-free polymeric photocatalyst for hydrogen production from water under visible light, *Nat. Mater.* 8 (2008) 76–80. doi:10.1038/nmat2317.
- [38] C. Yue, J. Jiang, M. Li, X. Wang, T. Li, Accelerating the peroxymonosulfate activation and charge transfer by construction of Fermi energy level-matched

- CoWO₄/g-C₃N₄ photocatalyst for typical antibiotics degradation, *Sep. Purif. Technol.* 301 (2022) 122020. doi:10.1016/j.seppur.2022.122020.
- [39] M. Wang, C. Jin, J. Kang, J. Liu, Y. Tang, Z. Li, S. Li, CuO/g-C₃N₄ 2D/2D heterojunction photocatalysts as efficient peroxymonosulfate activators under visible light for oxytetracycline degradation: Characterization, efficiency and mechanism, *Chem. Eng. J.* 416 (2021) 128118. doi:10.1016/j.cej.2020.128118.
- [40] Y. Gong, X. Zhao, H. Zhang, B. Yang, K. Xiao, T. Guo, J. Zhang, MOF-derived nitrogen doped carbon modified g-C₃N₄ heterostructure composite with enhanced photocatalytic activity for bisphenol A degradation with peroxymonosulfate under visible light irradiation, *Appl. Catal. B Environ.* 233 (2018) 35–45. doi:10.1016/j.apcatb.2018.03.077.
- [41] G. Alnagar, A. Hezam, Q.A. Drmosh, S. Ananda, Sunlight-driven activation of peroxymonosulfate by microwave synthesized ternary MoO₃/Bi₂O₃/g-C₃N₄ heterostructures for boosting tetracycline hydrochloride degradation, *Chemosphere.* 272 (2021) 129807. doi:10.1016/j.chemosphere.2021.129807.
- [42] J. Wang, M. Wang, J. Kang, Y. Tang, J. Liu, S. Li, Z. Xu, P. Tang, The promoted tetracycline visible-light-driven photocatalytic degradation efficiency of g-C₃N₄/FeWO₄ Z-scheme heterojunction with peroxymonosulfate assisting and mechanism, *Sep. Purif. Technol.* 296 (2022) 121440. doi:10.1016/j.seppur.2022.121440.
- [43] J. Jiang, X. Wang, C. Zhang, T. Li, Y. Lin, Porous 0D/3D NiCo₂O₄/g-C₃N₄ accelerate emerging pollutant degradation in PMS/vis system: Degradation mechanism, pathway and toxicity assessment, *Chem. Eng. J.* 397 (2020) 125356. doi:10.1016/j.cej.2020.125356.
- [44] Y. Peng, H. Tang, B. Yao, X. Gao, X. Yang, Y. Zhou, Activation of peroxymonosulfate (PMS) by spinel ferrite and their composites in degradation of organic pollutants: A Review, *Chem. Eng. J.* 414 (2021) 128800. doi:10.1016/j.cej.2021.128800.
- [45] X. Li, T. Chen, Y. Qiu, Z. Zhu, H. Zhang, D. Yin, Magnetic dual Z-scheme g-C₃N₄/BiVO₄/CuFe₂O₄ heterojunction as an efficient visible-light-driven peroxymonosulfate activator for levofloxacin degradation, *Chem. Eng. J.* 452 (2023) 139659. doi:10.1016/j.cej.2022.139659.
- [46] P. Sarkar, D. Roy, B. Bera, S. De Sudarsan, Enhanced photodegradation of reactive dyes in textile effluent with CoFe₂O₄/g-CN heterostructure-mediated

- peroxymonosulphate activation, *Environ. Sci. Pollut. Res.* 29 (2022) 50566–50583. doi:10.1007/s11356-022-18944-2.
- [47] B. Palanivel, V. Jayaraman, C. Ayyappan, M. Alagiri, Magnetic binary metal oxide intercalated g-C₃N₄ : Energy band tuned p-n heterojunction towards Z-scheme photo-Fenton phenol reduction and mixed dye degradation, *J. Water Process Eng.* 32 (2019) 100968. doi:10.1016/j.jwpe.2019.100968.
- [48] X. Sun, L. Huang, G. Wang, H. Feng, S. Zhou, R. Zhao, D. Wang, Z. Li, Efficient degradation of tetracycline under the conditions of high-salt and coexisting substances by magnetic CuFe₂O₄/g-C₃N₄ photo-Fenton process, *Chemosphere.* 308 (2022) 136204. doi:10.1016/j.chemosphere.2022.136204.
- [49] H. Sun, T. Zhou, J. Kang, Y. Zhao, Y. Zhang, T. Wang, High-efficient degradation of oxytetracycline by visible photo-Fenton process using MnFe₂O₄/g-C₃N₄ : Performance and mechanisms, *Sep. Purif. Technol.* 299 (2022) 121771. doi:10.1016/j.seppur.2022.121771.
- [50] M.M. Sablas, M.D.G. de Luna, S. Garcia-Segura, C.W. Chen, C.F. Chen, C. Di Dong, Percarbonate mediated advanced oxidation completely degrades recalcitrant pesticide imidacloprid: Role of reactive oxygen species and transformation products, *Sep. Purif. Technol.* 250 (2020) 117269. doi:10.1016/j.seppur.2020.117269.
- [51] C.M. Batikian, A. Lu, K. Watanabe, J. Pitt, R.M. Gersberg, Temporal pattern in levels of the neonicotinoid insecticide, imidacloprid, in an urban stream, *Chemosphere.* 223 (2019) 83–90. doi:10.1016/j.chemosphere.2019.01.165.
- [52] L.P. Belzunces, J.M. Bonmatin, M. Chagnon, C. Downs, Systemic insecticides (neonicotinoids and fipronil): trends , uses , mode of action and metabolites, *Environ. Sci. Pollut. Res.* 22 (2015) 5–34. doi:10.1007/s11356-014-3470-y.
- [53] D.A. Thompson, H.J. Lehmler, D.W. Kolpin, M.L. Hladik, J.D. Vargo, K.E. Schilling, G.H. Lefevre, T.L. Peeples, M.C. Poch, L.E. Laduca, D.M. Cwiertny, R.W. Field, A critical review on the potential impacts of neonicotinoid insecticide use: Current knowledge of environmental fate, toxicity, and implications for human health, *Environ. Sci. Process. Impacts.* 22 (2020) 1315–1346. doi:10.1039/c9em00586b.
- [54] M. Lamers, M. Anyusheva, N. La, V.V. Nguyen, T. Streck, Pesticide Pollution in Surface- and Groundwater by Paddy Rice Cultivation: A Case Study from Northern Vietnam, *Clean-Soil, Air, Water.* 39 (2011) 356–361.

- doi:10.1002/clen.201000268.
- [55] C.A. Morrissey, P. Mineau, J.H. Devries, F. Sanchez-Bayo, M. Liess, M.C. Cavallaro, K. Liber, Neonicotinoid contamination of global surface waters and associated risk to aquatic invertebrates: A review, *Environ. Int.* 74 (2015) 291–303. doi:10.1016/j.envint.2014.10.024.
- [56] C.M. Rocha, A.M. Lastre-Acosta, M.P.S. Parizi, A.C.S.C. Teixeira, Environmental photochemical fate of pesticides ametryn and imidacloprid in surface water (Paranapanema River, São Paulo, Brazil), *Environ. Sci. Pollut. Res.* 29 (2022) 42290–42304. doi:10.1007/s11356-021-17991-5.
- [57] J.C. Anderson, C. Dubetz, V.P. Palace, Neonicotinoids in the Canadian aquatic environment: A literature review on current use products with a focus on fate, exposure, and biological effects, *Sci. Total Environ.* 505 (2015) 409–422. doi:10.1016/j.scitotenv.2014.09.090.
- [58] Y. Ma, L. Wu, P. Li, L. Yang, L. He, S. Chen, Y. Yang, F. Gao, X. Qi, Z. Zhang, A novel, efficient and sustainable magnetic sludge biochar modified by graphene oxide for environmental concentration imidacloprid removal, *J. Hazard. Mater.* 407 (2021). doi:10.1016/j.jhazmat.2020.124777.
- [59] M. Kanwal, S.R. Tariq, G.A. Chotana, Photocatalytic degradation of imidacloprid by Ag-ZnO composite, *Environ. Sci. Pollut. Res.* 25 (2018) 27307–27320. doi:10.1007/s11356-018-2693-8.
- [60] M. Naghizadeh, M.A. Taher, A.M. Tamaddon, Facile synthesis and characterization of magnetic nanocomposite ZnO/CoFe₂O₄ hetero-structure for rapid photocatalytic degradation of imidacloprid, *Heliyon.* 5 (2019) e02870. doi:10.1016/j.heliyon.2019.e02870.
- [61] J. Li, W. Huang, L. Yang, G. Gou, C. Zhou, L. Li, N. Li, C. Liu, B. Lai, Novel Ag₃PO₄ modified tubular carbon nitride with visible-light-driven peroxy monosulfate activation: A wide pH tolerance and reaction mechanism, *Chem. Eng. J.* 432 (2022) 133588. doi:10.1016/j.cej.2021.133588.
- [62] J. Li, L. Yang, B. Lai, C. Liu, Y. He, G. Yao, N. Li, Recent progress on heterogeneous Fe-based materials induced persulfate activation for organics removal, *Chem. Eng. J.* 414 (2021) 128674. doi:10.1016/j.cej.2021.128674.
- [63] J. Li, G. Gou, H. Zhao, C. Liu, N. Li, L. Li, B. Tan, B. Lai, Efficient peroxy monosulfate activation by CoFe₂O₄-CeO₂ composite: Performance and catalytic mechanism, *Chem. Eng. J.* 435 (2022) 134840.

- doi:10.1016/j.cej.2022.134840.
- [64] G.P. Anipsitakis, D.D. Dionysiou, Radical generation by the interaction of transition metals with common oxidants, *Environ. Sci. Technol.* 38 (2004) 3705–3712. doi:10.1021/es035121o.
- [65] P.R. Shukla, S. Wang, H. Sun, H.M. Ang, M. Tadé, Activated carbon supported cobalt catalysts for advanced oxidation of organic contaminants in aqueous solution, *Appl. Catal. B Environ.* 100 (2010) 529–534. doi:10.1016/j.apcatb.2010.09.006.
- [66] T. Ni, Z. Yang, H. Zhang, L. Zhou, W. Guo, L. Pan, Z. Yang, K. Chang, C. Ge, D. Liu, Peroxymonosulfate activation by $\text{Co}_3\text{O}_4/\text{SnO}_2$ for efficient degradation of ofloxacin under visible light, *J. Colloid Interface Sci.* 615 (2022) 650–662. doi:10.1016/j.jcis.2022.02.024.
- [67] L. Valenzuela, A. Iglesias, M. Faraldos, A. Bahamonde, R. Rosal, Antimicrobial surfaces with self-cleaning properties functionalized by photocatalytic ZnO electrospayed coatings, *J. Hazard. Mater.* 369 (2019) 665–673. doi:10.1016/j.jhazmat.2019.02.073.
- [68] C. Adán, A. Martínez-Arias, M. Fernández-García, A. Bahamonde, Photocatalytic degradation of ethidium bromide over titania in aqueous solutions, *Appl. Catal. B Environ.* 76 (2007) 395–402. doi:10.1016/j.apcatb.2007.06.013.
- [69] S.-H. Chai, H.-P. Wang, Y. Liang, B.-Q. Xu, Sustainable production of acrolein: Gas-phase dehydration of glycerol over Nb_2O_5 catalyst, *J. Catal.* 250 (2007) 342–349. doi:10.1016/j.jcat.2007.06.016.
- [70] M. Aadil, S. Zulfiqar, M.F. Warsi, P.O. Agboola, I. Shakir, M. Shahid, N.F. Al-Khalli, Mesoporous and macroporous Ag-doped Co_3O_4 nanosheets and their superior photo-catalytic properties under solar light irradiation, *Ceram. Int.* 47 (2021) 9806–9817. doi:10.1016/j.ceramint.2020.12.121.
- [71] A. Gulino, P. Dapporto, P. Rossi, I. Fragala, A Novel Self-generating Liquid MOCVD Precursor for Co_3O_4 Thin Films, *Chem. Mater.* 15 (2003) 3748–3752. doi:10.1021/cm034305z.
- [72] J. Liu, D. Wang, M. Wang, D. Kong, Y. Zhang, J.F. Chen, L. Dai, Uniform Two-Dimensional Co_3O_4 Porous Sheets: Facile Synthesis and Enhanced Photocatalytic Performance, *Chem. Eng. Technol.* 39 (2016) 891–898. doi:10.1002/ceat.201500542.
- [73] P. Praus, On electronegativity of graphitic carbon nitride, *Carbon N. Y.* 172 (2021)

- 729–732. doi:10.1016/j.carbon.2020.10.074.
- [74] M. Long, W. Cai, J. Cai, B. Zhou, X. Chai, Y. Wu, Efficient photocatalytic degradation of phenol over $\text{Co}_3\text{O}_4/\text{BiVO}_4$ composite under visible light irradiation, *J. Phys. Chem. B.* 110 (2006) 20211–20216. doi:10.1021/jp063441z.
- [75] A.C. Nogueira, L.E. Gomes, J.A.P. Ferencz, J.E.F.S. Rodrigues, R. V. Gonçalves, H. Wender, Improved Visible Light Photoactivity of $\text{CuBi}_2\text{O}_4/\text{CuO}$ Heterojunctions for Photodegradation of Methylene Blue and Metronidazole, *J. Phys. Chem. C.* 123 (2019) 25680–25690. doi:10.1021/acs.jpcc.9b06907.
- [76] Q. Wang, P. Rao, G. Li, L. Dong, X. Zhang, Y. Shao, N. Gao, W. Chu, B. Xu, N. An, J. Deng, Degradation of imidacloprid by UV-activated persulfate and peroxymonosulfate processes: Kinetics, impact of key factors and degradation pathway, *Ecotoxicol. Environ. Saf.* 187 (2020) 109779. doi:10.1016/j.ecoenv.2019.109779.
- [77] L. Zishun, X. Tanga, G. Huanga, X. Luoc, D. Hed, Q. Penga, J. Huanga, M. Aoa, K. Liu, Bismuth MOFs based hierarchical $\text{Co}_3\text{O}_4\text{-Bi}_2\text{O}_3$ composite: An efficient heterogeneous peroxymonosulfate activator for azo dyes degradation, *Sep. Purif. Technol.* 242 (2020) 116825. doi:10.1016/j.seppur.2020.116825.
- [78] H. Zhang, L. chao Nengzi, X. Li, Z. Wang, B. Li, L. Liu, X. Cheng, Construction of $\text{CuBi}_2\text{O}_4/\text{MnO}_2$ composite as Z-scheme photoactivator of peroxymonosulfate for degradation of antibiotics, *Chem. Eng. J.* 386 (2020) 124011. doi:10.1016/j.cej.2020.124011.
- [79] S. Liu, Z. Zhang, F. Huang, Y. Liu, L. Feng, J. Jiang, L. Zhang, F. Qi, C. Liu, Carbonized polyaniline activated peroxymonosulfate (PMS) for phenol degradation: Role of PMS adsorption and singlet oxygen generation, *Appl. Catal. B Environ.* 286 (2021) 119921. doi:10.1016/j.apcatb.2021.119921.
- [80] M.M. Mian, G. Liu, Activation of peroxymonosulfate by chemically modified sludge biochar for the removal of organic pollutants: Understanding the role of active sites and mechanism, *Chem. Eng. J.* 392 (2020) 123681. doi:10.1016/j.cej.2019.123681.
- [81] J. Guo, C.H. Shen, J. Sun, X.J. Xu, X.Y. Li, Z.H. Fei, Z.T. Liu, X.J. Wen, Highly efficient activation of peroxymonosulfate by $\text{Co}_3\text{O}_4/\text{Bi}_2\text{MoO}_6$ p-n heterostructure composites for the degradation of norfloxacin under visible light irradiation, *Sep. Purif. Technol.* 259 (2021) 118109. doi:10.1016/j.seppur.2020.118109.
- [82] Y. Jiang, Z. Wang, J. Huang, F. Yan, Y. Du, C. He, Y. Liu, G. Yao, B. Lai, A

- singlet oxygen dominated process through photocatalysis of CuS-modified MIL-101(Fe) assisted by peroxymonosulfate for efficient water disinfection, *Chem. Eng. J.* 439 (2022) 135778. doi:10.1016/j.cej.2022.135788.
- [83] D. García-Fresnadillo, Singlet Oxygen Photosensitizing Materials for Point-of-Use Water Disinfection with Solar Reactors, *ChemPhotoChem.* 2 (2018) 512–534. doi:10.1002/cptc.201800062.
- [84] J. Fan, H. Qin, S. Jiang, Mn-doped g-C₃N₄ composite to activate peroxymonosulfate for acetaminophen degradation: The role of superoxide anion and singlet oxygen, *Chem. Eng. J.* 359 (2019) 723–732. doi:10.1016/j.cej.2018.11.165.
- [85] Y.H. Guan, J. Ma, X.C. Li, J.Y. Fang, L.W. Chen, Influence of pH on the formation of sulfate and hydroxyl radicals in the UV/Peroxymonosulfate system, *Environ. Sci. Technol.* 45 (2011) 9308–9314. doi:10.1021/es2017363.
- [86] X. Liu, T. Zhang, Y. Zhou, L. Fang, Y. Shao, Degradation of atenolol by UV/peroxymonosulfate: Kinetics, effect of operational parameters and mechanism, *Chemosphere.* 93 (2013) 2717–2724. doi:10.1016/j.chemosphere.2013.08.090.
- [87] M.L. Dell’Arciprete, L. Santos-Juanes, A. Arques, R.F. Vercher, A.M. Amat, J.P. Furlong, D.O. Mártire, M.C. Gonzalez, Reactivity of neonicotinoid pesticides with singlet oxygen, *Catal. Today.* 151 (2010) 137–142. doi:10.1016/j.cattod.2010.01.020.
- [88] T. Roberts and D. Hutson, *Metabolic Pathways of Agrochemicals: Part 2, Insecticides and Fungicides*, The Royal Society of Chemistry, Cornwall, UK, 1999. doi: 10.1039/9781847551375-00937.
- [89] D. Mohanta, M. Ahmaruzzaman, Au–SnO₂–CdS ternary nanoheterojunction composite for enhanced visible light-induced photodegradation of imidacloprid, *Environ. Res.* 201 (2021) 111586. doi:10.1016/j.envres.2021.111586.
- [90] C.F.Z. Lacson, M.D.G. de Luna, C. Dong, S. Garcia-Segura, M.C. Lu, Fluidized-bed Fenton treatment of imidacloprid: Optimization and degradation pathway, *Sustain. Environ. Res.* 28 (2018) 309–314. doi:10.1016/j.serj.2018.09.001.
- [91] C. Zhang, F. Li, H. Zhang, R. Wen, X. Yi, Y. Yang, J. He, G.G. Ying, M. Huang, Crucial roles of 3D–MoO₂–PBC cocatalytic electrodes in the enhanced degradation of imidacloprid in heterogeneous electro–Fenton system: Degradation mechanisms and toxicity attenuation, *J. Hazard. Mater.* 420 (2021).

- doi:10.1016/j.jhazmat.2021.126556.
- [92] M. Voigt, V. Langerbein, M. Jaeger, In silico ecotoxicity assessment of photoinduced imidacloprid degradation using HPLC–HRMS, QSAR and ecotoxicity equivalents, *Environ. Sci. Eur.* 34 (2022). doi:10.1186/s12302-022-00616-0.
- [93] Q. Kan, K. Lu, S. Dong, D. Shen, Q. Huang, Y. Tong, W. Wu, S. Gao, L. Mao, Transformation and removal of imidacloprid mediated by silver ferrite nanoparticle facilitated peroxymonosulfate activation in water: Reaction rates, products, and pathways, *Environ. Pollut.* 267 (2020) 115438. doi:10.1016/j.envpol.2020.115438.
- [94] Q. Sun, Y. Zhao, J. Zhang, J. Sheng, Efficient degradation of antibiotics over Co(II)-doped Bi₂MoO₆ nanohybrid via the synergy of peroxymonosulfate activation and photocatalytic reaction under visible irradiation, *Chemosphere.* 302 (2022) 134807. doi:10.1016/j.chemosphere.2022.134807.
- [95] Q. Yi, J. Tan, W. Liu, H. Lu, M. Xing, J. Zhang, Peroxymonosulfate activation by three-dimensional cobalt hydroxide/graphene oxide hydrogel for wastewater treatment through an automated process, *Chem. Eng. J.* 400 (2020) 125965. doi:10.1016/j.cej.2020.125965.
- [96] X. Ao, W. Sun, S. Li, C. Yang, C. Li, Z. Lu, Degradation of tetracycline by medium pressure UV-activated peroxymonosulfate process: Influencing factors, degradation pathways, and toxicity evaluation, *Chem. Eng. J.* 361 (2019) 1053–1062. doi:10.1016/j.cej.2018.12.133.
- [97] R.R.M. Silva, L. Valenzuela, R. Rosal, L.A.M. Ruotolo, F.G.E. Nogueira, A. Bahamonde, Peroxymonosulfate activation by Co₃O₄ coatings for imidacloprid degradation in a continuous flow-cell reactor under simulated solar irradiation, *J. Environ. Chem. Eng.* 11 (2023) 109265. doi:10.1016/j.jece.2023.109265.
- [98] Q. Sun, X. Wang, Y. Liu, Y. Zhang, S. Xia, J. Zhao, Visible-light-driven g-C₃N₄ doped CuFe₂O₄ floating catalyst enhanced peroxymonosulfate activation for sulfamethazine removal via singlet oxygen and high-valent metal-oxo species, *Chem. Eng. J.* 455 (2023) 140198. doi:10.1016/j.cej.2022.140198.
- [99] Y. Wang, H. Duan, H. Li, J. Zhen, W. Lv, Efficient activation of peroxymonosulfate by MoS₂ intercalated MgCuFe layered double hydroxide for phenol pollutant control, *J. Environ. Chem. Eng.* 11 (2023) 109502. doi:10.1016/j.jece.2023.109502.

- [100] M. Ismael, The photocatalytic performance of the ZnO/g-C₃N₄ composite photocatalyst toward degradation of organic pollutants and its inactivity toward hydrogen evolution : The influence of light irradiation and charge transfer, *Chem. Phys. Lett.* 739 (2020) 136992. doi:10.1016/j.cplett.2019.136992.
- [101] K.T.G. Carvalho, A.E. Nogueira, O.F. Lopes, G. Byzinski, C. Ribeiro, Synthesis of g-C₃N₄/Nb₂O₅ heterostructures and their application in the removal of organic pollutants under visible and ultraviolet irradiation, *Ceram. Int.* 43 (2017) 3521–3530. doi:10.1016/j.ceramint.2016.11.063.
- [102] C. Jin, M. Wang, Z. Li, J. Kang, Y. Zhao, J. Han, Z. Wu, Two dimensional Co₃O₄/g-C₃N₄ Z-scheme heterojunction: Mechanism insight into enhanced peroxymonosulfate-mediated visible light photocatalytic performance, *Chem. Eng. J.* 398 (2020) 125569. doi:10.1016/j.cej.2020.125569.
- [103] L. Liu, J. Huang, H. Yu, J. Wan, L. Liu, K. Yi, Construction of MoO₃ nanoparticles/g-C₃N₄ nanosheets 0D/2D heterojunction photocatalysts for enhanced photocatalytic degradation of antibiotic pollutant, *Chemosphere.* 282 (2021) 131049. doi:10.1016/j.chemosphere.2021.131049.
- [104] S. Yan, Y. Shi, Y. Tao, H. Zhang, Enhanced persulfate-mediated photocatalytic oxidation of bisphenol A using bioelectricity and a g-C₃N₄/Fe₂O₃ heterojunction, *Chem. Eng. J.* 359 (2019) 933–943. doi:10.1016/j.cej.2018.11.093.
- [105] S. Kumar, A. Kumar, G. Sharma, M. Naushad, M. Ubaidullah, A. García-pe, Developing a g-C₃N₄/NiFe₂O₄ S-scheme hetero-assembly for efficient photocatalytic degradation of cephalexin, *Colloids Surfaces A Physicochem. Eng. Asp.* 654 (2022). doi:10.1016/j.colsurfa.2022.129968.
- [106] X. Zhang, Y. Gao, Y. Li, Y. Zhou, H. Ma, J. Shang, Synthesis of magnetic NiFe₂O₄/CuS activator for degradation of lomefloxacin via the activation of peroxymonosulfate under simulated sunlight illumination, *Sep. Purif. Technol.* 288 (2022) 120664. doi:10.1016/j.seppur.2022.120664.
- [107] S. Liu, A. Zada, X. Yu, F. Liu, G. Jin, NiFe₂O₄/g-C₃N₄ heterostructure with an enhanced ability for photocatalytic degradation of tetracycline hydrochloride and antibacterial performance, *Chemosphere.* 307 (2022) 135717. doi:10.1016/j.chemosphere.2022.135717.
- [108] D. Sun, J. Mao, L. Cheng, X. Yang, H. Li, L. Zhang, W. Zhang, Magnetic g-C₃N₄/NiFe₂O₄ composite with enhanced activity on photocatalytic disinfection of *Aspergillus flavus*, *Chem. Eng. J.* 418 (2021) 129417.

- doi:10.1016/j.cej.2021.129417.
- [109] H. Ji, X. Jing, Y. Xu, J. Yan, H. Li, Y. Li, L. Huang, Q. Zhang, H. Xu, H. Li, Magnetic g-C₃N₄/NiFe₂O₄ hybrids with enhanced photocatalytic activity, *RSC Adv.* 5 (2015) 57960–57967. doi:10.1039/c5ra07148h.
- [110] H. Pang, Y. Jiang, W. Xiao, Y. Ding, C. Lu, Z. Liu, P. Zhang, H. Luo, W. Qin, Facile synthesis of few-layer g-C₃N₄ nanosheets anchored with cubic-phase CdS nanocrystals for high photocatalytic hydrogen generation activity, *J. Alloys Compd.* 839 (2020) 155684. doi:10.1016/j.jallcom.2020.155684.
- [111] X. Sun, L. Huang, G. Wang, H. Feng, S. Zhou, R. Zhao, D. Wang, Z. Li, Efficient degradation of tetracycline under the conditions of high-salt and coexisting substances by magnetic CuFe₂O₄/g-C₃N₄ photo-Fenton process, *Chemosphere.* 308 (2022) 136204. doi:10.1016/j.chemosphere.2022.136204.
- [112] B. Palanivel, C. Hu, M. Shkir, S. Alfaify, F.A. Ibrahim, M.S. Hamdy, A. Mani, Fluorine doped g-C₃N₄ coupled NiFe₂O₄ heterojunction: Consumption of H₂O₂ for production of hydroxyl radicals towards paracetamol degradation, *Colloid Interface Sci. Commun.* 42 (2021) 100410. doi:10.1016/j.colcom.2021.100410.
- [113] J. Guo, X. Li, Z. Chen, J. Zhu, X. Mai, R. Wei, K. Sun, H. Liu, Y. Chen, N. Naik, Z. Guo, Magnetic NiFe₂O₄/Polypyrrole nanocomposites with enhanced electromagnetic wave absorption, *J. Mater. Sci. Technol.* 108 (2022) 64–72. doi:10.1016/j.jmst.2021.08.049.
- [114] J. Cao, C. Qin, Y. Wang, H. Zhang, G. Sun, Z. Zhang, Solid-State Method Synthesis of SnO₂-Decorated g-C₃N₄ Nanocomposites with Enhanced Gas-Sensing Property to Ethanol, *Materials (Basel).* 10 (2017) 604. doi:10.3390/ma10060604.
- [115] X. Guo, S. Ai, D. Yang, L. Zhao, H. Ding, Synergistic photocatalytic and Fenton-like degradation of organic contaminants using peroxydisulfate activated by CoFe₂O₄@g-C₃N₄ composite, *Environ. Technol.* 42 (2021) 2240–2253. doi:10.1080/09593330.2019.1697378.
- [116] M. Moradi, B. Kakavandi, A. Bahadoran, S. Giannakis, Intensification of persulfate-mediated elimination of bisphenol A by a spinel cobalt ferrite-anchored g-C₃N₄ S-scheme photocatalyst: Catalytic synergies and mechanistic interpretation, *Sep. Purif. Technol.* 285 (2022) 120313. doi:10.1016/j.seppur.2021.120313.
- [117] C. Han, L. Ge, C. Chen, Y. Li, X. Xiao, Novel visible light induced Co₃O₄-g-C₃N₄

- heterojunction photocatalysts for efficient degradation of methyl orange, *Appl. Catal. B, Environ.* 147 (2014) 546–553. doi:10.1016/j.apcatb.2013.09.038.
- [118] R. Tang, D. Gong, Y. Deng, S. Xiong, J. Zheng, L. Li, π - π stacking derived from graphene-like biochar/g-C₃N₄ with tunable band structure for photocatalytic antibiotics degradation via peroxymonosulfate activation, *J. Hazard. Mater.* 423 (2022) 126944. doi:10.1016/j.jhazmat.2021.126944.
- [119] X. Dou, Y. Chen, H. Shi, CuBi₂O₄/BiOBr composites promoted PMS activation for the degradation of tetracycline : S-scheme mechanism boosted Cu²⁺/Cu⁺ cycle, *Chem. Eng. J.* 431 (2022) 134054. doi:10.1016/j.cej.2021.134054.
- [120] X. Jiang, K. Xiao, Z. Liu, W. Xu, F. Liang, S. Mo, X. Wu, J. Beiyuan, Novel 0D-1D-2D nanostructured MCN/NCDs recyclable composite for boosted peroxymonosulfate activation under visible light toward tetracycline degradation, *Sep. Purif. Technol.* 296 (2022) 121328. doi:10.1016/j.seppur.2022.121328.
- [121] H. Guo, H. Niu, C. Liang, C. Niu, Y. Liu, N. Tang, Y. Yang, Few-layer graphitic carbon nitride nanosheet with controllable functionalization as an effective metal-free activator for peroxymonosulfate photocatalytic activation : Role of the energy band bending, *Chem. Eng. J.* 401 (2020) 126072. doi:10.1016/j.cej.2020.126072.
- [122] Y. Zhao, B. Li, Y. Li, X. Fan, F. Zhang, G. Zhang, Q. Xia, W. Peng, Synergistic activation of peroxymonosulfate between Co and MnO for bisphenol A degradation with enhanced activity and stability, *J. Colloid Interface Sci.* 623 (2022) 775–786. doi:10.1016/j.jcis.2022.05.105.
- [123] J. Ye, D. Yang, J. Dai, C. Li, Y. Yan, Y. Wang, Strongly coupled cobalt / oxygen co-doped porous g-C₃N₄ heterostructure with abundant oxygen vacancies modulated the peroxymonosulfate activation pathway, *Chem. Eng. J.* 431 (2022) 133972. doi:10.1016/j.cej.2021.133972.
- [124] Y. Xu, J. Ai, H. Zhang, The mechanism of degradation of bisphenol A using the magnetically separable CuFe₂O₄/peroxymonosulfate heterogeneous oxidation process, *J. Hazard. Mater.* 309 (2016) 87–96. doi:10.1016/j.jhazmat.2016.01.023.
- [125] Y. Zhou, X. Wang, C. Zhu, D.D. Dionysiou, G. Zhao, G. Fang, D. Zhou, New insight into the mechanism of peroxymonosulfate activation by sulfur-containing minerals : Role of sulfur conversion in sulfate radical generation, *Water Res.* 142 (2018) 208–216. doi:10.1016/j.watres.2018.06.002.